Master of Science

Study of fluorine substitution effect at oxygen site of $LiFeBO_3$ cathode material for lithium-ion battery

The Graduate School of the University of Ulsan

Department of Chemistry

Khoirul Umam

Study of fluorine substitution effect at oxygen site of $LiFeBO_3$ cathode material for lithium-ion battery

Supervisor Professor Youngil Lee

A Dissertation

Submitted to

The Graduate School of the University of Ulsan

In partial fulfillment of the requirements

for the degree of

Master of Science

by

Khoirul Umam

Department of Chemistry

University of Ulsan, Ulsan, Korea

January 2020

Study of fluorine substitution effect at oxygen site of $LiFeBO_3$ cathode material for lithium-ion battery

This certifies that the dissertation of Khoirul Umam is approved.

Committee Chair Dr. Jiwon Ha

Committee Member Dr. Jaehoon Jung

Committee Member Dr. Youngil Lee

Department of Chemistry

Ulsan, Korea

January 2020

Abstract

Fluorine substituted $LiFeBO_3$ at oxygen site, $LiFeBO_{3-x}F_{2x}$ (LFeBF, x = 0, 0.05, 0.1, 0.2, 0.3, and 0.5), have been synthesized by solid-state reaction method to improve electrochemical properties as a cathode material of lithium-ion batteries. The structural studies of LFeBF depending on fluorine substitution ratio have been performed with X-ray diffraction (XRD) and ^{7}Li magic angle spinning (MAS) nuclear magnetic resonance (NMR) spectroscopy, which results show the structure of samples are changed from monoclinic to vonsenite. The morphology and elemental maps have been observed by scanning electron microscopy (SEM) combined energy dispersive X-ray (EDX) spectrometer. The SEM images of LFeBF showed the morphology change with increasing fluorine substitution ratio. The electrochemical study is performed by galvanostatic charge and discharge test with the potential range of 1.0 – 4.5 V. The results have shown that fluorine substitution at oxygen site of $LiFeBO_3$ has effectively improved electrochemical performance with the highest discharge capacity of 363.98 mAh g^{-1} at 0.05 C rate for LFeBF (x = 0.3).

Contents

List of tables

List of figures

1. Introduction

1.1 Lithium-ion battery

1.1.1 History of lithium-ion battery

Lithium-ion batteries (LIBs) are extensively employed as power sources in a wide range of applications owing to their high energy densities, high coulombic efficiencies, low self-discharge features, and a range of chemical potentials accessible with diverse electrode designs. For the past decade, there has been a growing trend towards next-generation LIBs with high charge capacities and power densities developed for electric vehicles (EVs), hybrid electric vehicles (HEVs), energy storage system (ESS) [1], aerospace applications, and autonomous electric devices such hybrid solar batteries [2]. In the beginning, the integration of Li metals in anode relied on several advantageous properties of Li metal is such as the electropositivity , about –3.04 V versus standard hydrogen electrode, as well as the lightest metal with equivalent weight M = 46.94 g mol^{-1}, and specific gravity ρ = 40.53 g cm^{-3}, thus promotingthe development of storage systems with high energy density [3]. The LIBs are a kind of rechargeable batteries with the highest energy density developed so far [4]. The energy density of the developed LIBs can be as high as 250 Wh kg^{-1} and its life cycle can reach more than 10.000 cycles depending on the working conditions [4]. The history of the current rechargeable LIBs was started from

rechargeable Li metal battery (LMB) and the initiator of a cell that resembled a secondary LMB was Lewis and Keyes in 1913 [5]. The advantage of Li metal was reported in the 1970s with the assembly of primary Li cells [3]. Owing to the high capacity and variable discharge rate, they rapidly used as power sources for watches, calculators or for implantable medical devices [3]. About 30 years ago Sony Co. commercialized the world's first LIBs [5]. And **Table 1.1** shows the summary of the lithium batteries history until 2010 [6].

Year	Cell	Author
1972	Lithium primary battery Li/organic electrolyte/CFx	Matsushita
1972	Solid lithium iodine battery Li/LiI/I-PVP	Moser
1977	Rechargeable lithium battery Li/organic electrolyte/TiS_2	Whittingham
1978	Polymer electrolyte battery Li/PEO electrolyte/V_2O_5	Armand
1980	First lithium-ion cathode $LiCoO_2$	Goodenough
1980	Rocking chair battery Li_xWO_2/organic electrolyte/TiS_2	Scrosati
1991	Lithium-ion battery C/organic electrolyte/$LiCoO_2$	Sony
1996	Lithium-air battery Li/organic electrolyte/O_2,C	Abraham
1997	Olivine type cathode $LiFePO_4$	Goodenough
2006	Lithium-air battery Li/film/acquisition /O_2,C	Visco
2006	Lithium-air battery Li/film/acquisition /O_2,C, catalyst	Bruce
2009	Lithium-sulfur battery Li/organic electrolyte/S,C	Nazar
2010	Lithium-ion sulfur battery Sn-C/organic electrolyte/Li_2S,C	Hassoun-Scrosati

Table 1.1 History of lithium-ion batteries [6]

1.1.2 Principle of lithium-ion battery

Figure 1.1 shows the schematic representation of typical LIBs with the main component. As can be seen, a lithium-ion battery is composed of four main components, namely the anode, cathode, electrolyte, and separator [7]. The anode material is usually composed of graphite, cathode material is usually composed of $LiMO_2$, with M is transition metal and for electrolyte usually used Li^+-containing salt [8]. During charging process, Li^+ ions move from the cathode to the anode through the electrolyte and separator. On the other hand, during the discharging process, the Li^+ ion migrates from anode to cathode, that provokes a simultaneous flow of the electrons out of the external circuit to provide the electrical power [7]. The transfer of Li^+ ions during charge and discharge is facilitated by a Li^+-containing salt in the electrolyte. The principle of charge and discharge process of LIBs showed in **Figure 1.2**. The electrochemical reactions in LIBs are:

$$LiMO_2 \rightleftarrows Li_{1-x}MO_2 + xLi^+ + xe^- \quad \text{(at the cathode)}$$

(Equation 1.1)

$$xLi^+ + xe^- + xC_6 \leftrightarrows xLiC_6 \quad \text{(at the anode)}$$

(Equation 1.2)

The overall cell reaction is:

$$LiMO_2 + C_6 \rightleftarrows Li_{1-x}MO_2 + Li_xC_6 \ (x = 0.5,\ V \sim 3.7 \text{ volts}) \quad \text{(Equation 1.3)}$$

As metallic Li is not present in this cell, Li-ion batteries are chemically less reactive, safer, and offer longer cycle life than rechargeable lithium batteries using Li metal as anodes [8]

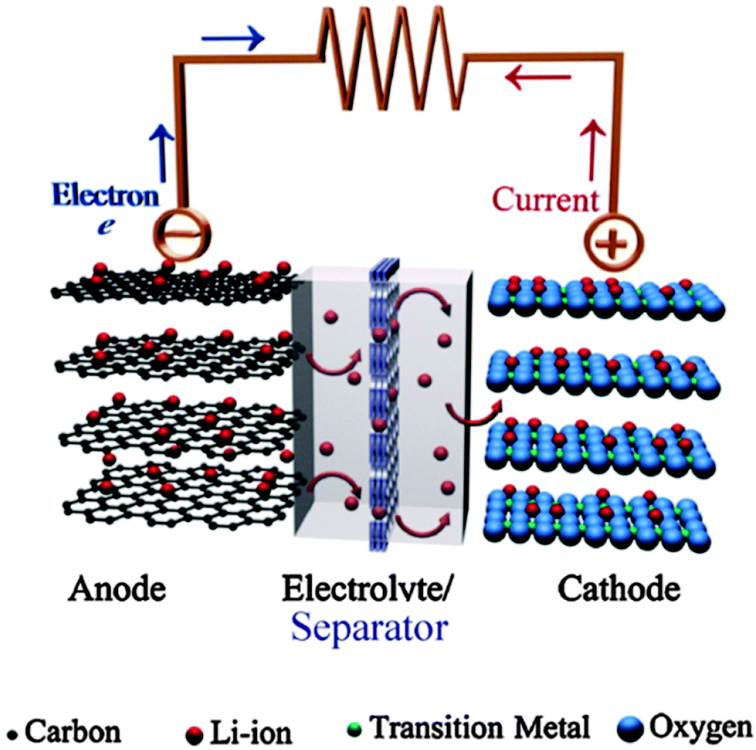

Figure 1.1 Schematic representation of a typical lithium-ion battery [8]

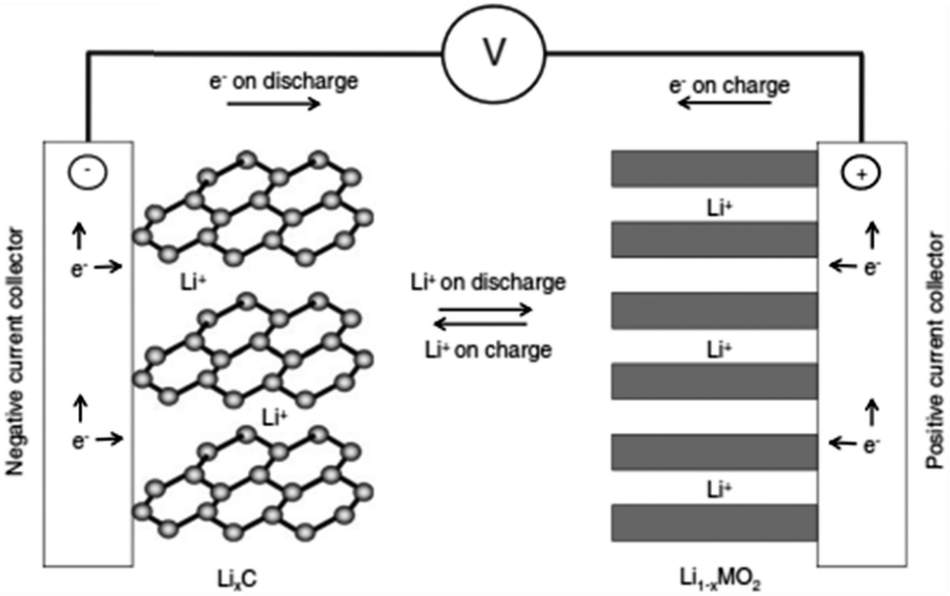

Figure 1.2 Scheme of the electrochemical process in a Li-ion battery [8]

In order to reach higher performance in rechargeable non-aqueous LIBs, a huge amount of attention have been devoted in the design of a cathode with a chemical potential (μ_C) that matches the HOMO of the electrolyte as well as an anode with a chemical potential (μ_A) that matches the LUMO of the electrolyte. Besides that, it is important to design a non-aqueous electrolyte with high Li^+ ion conductivity over the practical ambient temperature range, that has a potential window that allows a thermodynamically stable open-circuit voltage V_{OC} ≥ 4 V [8]. As mentioned above, one of the ways to improve the performance of LIBs is designing the anode material. And to enable the application of new types of electrode materials with high performance, various strategies have been used and summarized in **Figure 1.3** [9].

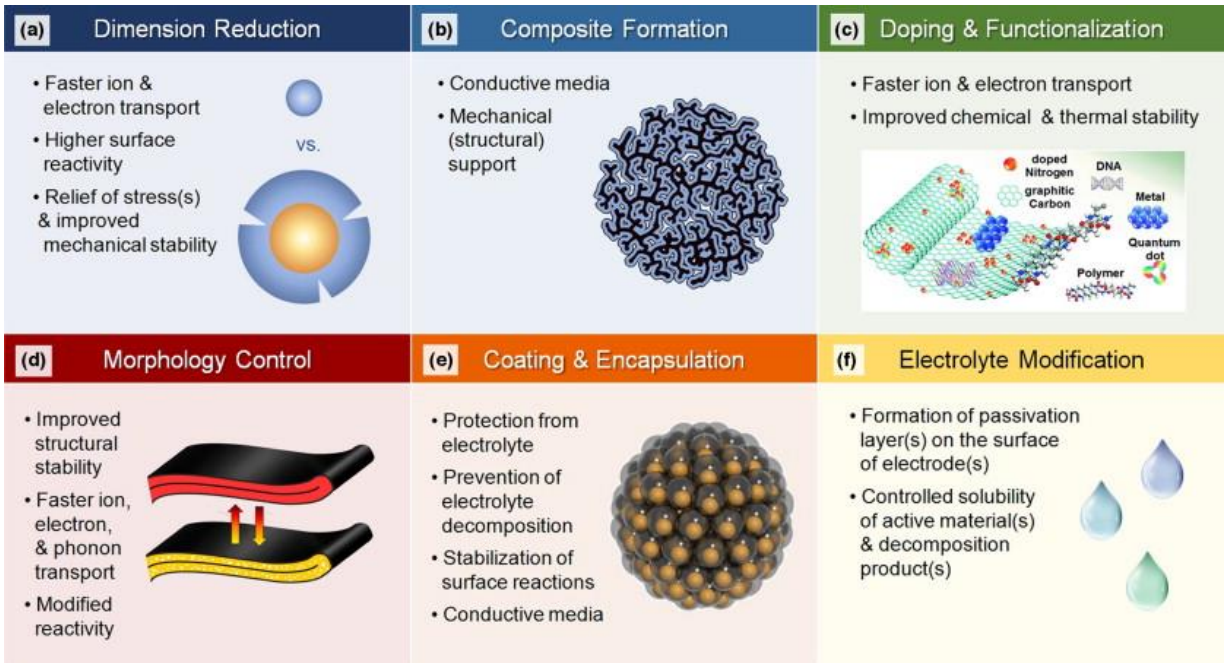

Figure 1.3 General strategies for performance enhancement and their rationale: (a) reducing dimensions of active materials, (b) formation of composites, (c) doping and functionalization, (d) tuning particle morphology, (e) formation of coatings or shells around active materials, (f) modification of electrolyte [9].

1.1.3 Cathode Material

The cathode is one of the important components of LIBs. The cathode material must have a stable crystalline over wide ranges of composition because, during the charging cycle, the oxidation reaction leads to large compositional changes and therefore to unfavorable phase changes [10, 11]. Cathode materials can store energy through two different mechanisms: intercalation and conversion reaction. Conversion electrodes undergo a solid-state redox reaction during lithiation/delithiation, in which there is a change in the crystalline structure, accompanied by the breaking and recombining chemical bonds [9, 11]. An intercalation cathode is a solid host network, which can store guest ions. The guest ions can be inserted into and be removed from the host network reversibly [9], where the reaction that occurs at the cathode material is the intercalation of Li ions into the host during the discharging process with spontaneous process, and deintercalation of Li ions from the host during the charging process with nonspontaneous process. Here, the term intercalation is used to describe the interaction process, whether it is true intercalation into a crystal void (van der Walls space) or between atomic planes, or whether it refers to alloying [8].

In a LIB, Li^+ is the guest ion and the host network compounds are metal chalcogenides, transition metal oxides, and polyanion compounds. These intercalation compounds can be divided into several crystal structures, such as layered, spinel, olivine, and tavorite, as shown in **Figure 1.4 (a-d)**. The layered

structure is the earliest form of intercalation compounds for the cathode materials in LIBs.

Current intercalation cathode research is focused on the transition metal oxide and polyanion compounds due to their higher operating voltage and the resulting higher energy storage capability. Typically, intercalation cathodes have 100–200 mAh g^{-1} specific capacity and 3–5 V average voltage vs. Li/Li^{+} as summarized in **Figure 1.4 (e)** [9].

The key requirements for a material to be successfully used as a cathode in a rechargeable LIBs [12] are as follows :

(1) The material contains a readily reducible/oxidizable ion, for example, a transition metal.

(2) The material reacts with lithium in a reversible manner.

  (a) This dictates an intercalation-type reaction in which the host structure essentially does not change as lithium is added.

(3) The material reacts with lithium with the high free energy of the reaction.

  (a) High capacity, preferably at least one lithium per transition metal.

  (b) High voltage, preferably around 4 V (as limited by the stability of electrolyte).

  (c) This leads to high-energy storage.

(4) The material reacts with lithium very rapidly both on insertion and removal.

(a) This leads to high power density, which is needed to replace the Ni/Cd battery or for batteries that can be recharged using HEV regenerative braking.

(5) The material is a good electronic conductor, preferably a metal.

(a) This allows for the easy addition or removal of electrons during the electrochemical reaction.

(b) This allows for the reaction at all contact points between the cathode active material and the electrolyte rather than at ternary contact points between the cathode active material, the electrolyte, and the electronic conductor (such as carbon black).

(c) This minimizes the need for inactive conductive diluents, which take away from the overall energy density.

(6) The material is stable, i.e., not change the structure or otherwise degrade, to over-discharge and overcharge.

(7) The material is low cost.

(8) The material is environmentally benign.

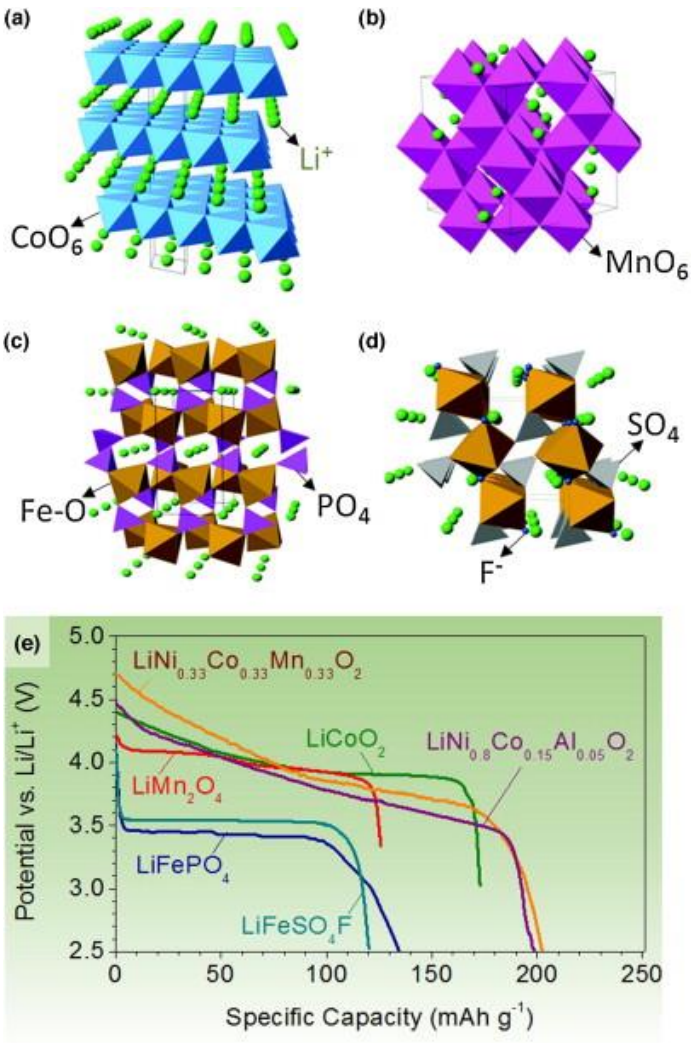

Figure 1.4 Crystal structures and discharge profiles of representative intercalation cathodes: structure of (a) layered ($LiCoO_2$), (b) spinel ($LiMn_2O_4$), (c) olivine ($LiFePO_4$), and (d) tavorite ($LiFeSO_4F$) and (e) typical discharge profiles of intercalation cathodes [9].

1.1.4 Polyanion cathode material

Polyanion compounds are a class of materials in which tetrahedral polyanion structure units $(XO^4)^{n-}$ and their derivatives $(X_mO_{3m+1})^{n-}$ (X = P, S, As, Mo, or W) with strong covalent bonding combine with MO_x (M = transition metal) polyhedral [4, 9]. As a new class of cathode materials for LIBs, polyanion compounds have attracted great interest since the first report on the electrochemical performance of $LiFePO_4$ by *Padhi et al.* [13]. **Table 1.2** summarizes some properties of polyanion compounds that have been investigated up to now [4]. Polyanion cathode materials possess higher thermal stability than conventional used layered transition metal oxides due to the strong covalently bonded oxygen atoms, which make them more suitable for large-scale LIB applications, by virtue of their better safety properties [4, 9].

Although polyanions show a lot of advantages as cathode materials for LIBs, the polyanion groups also bring some inactive mass into the electrode resulting in a relatively low theoretical capacity of polyanion compounds (such as 170 mAh/g for $LiFePO_4$), which lowers both the specific capacity and the specific energy. In this regard, , the development of borate-based cathode materials would be very attractive due to the low mass of $(BO_3)^{3-}$ polyanion group [4].

Polyanion	Compound	Structure	Voltage/ V (*vs* Li)	Theoretical capacity / practical capacity (mAh/g)	Thermal stability
Phosphates	$LiFePO_4$	Olivine strutur, orthorhombic (space group *Pmnb*)	3.5	170/> 160	Excelleent
	$LiMnPO_4$		4.1	171/160	Good
	$LiCoPO_4$		4.8	167/120	Poor
	$LiNiPO_4$		5.1	169 (no data)	\
Silicates	Li_2FeSiO_4	Li3PO4 structure, tetrahedral (as much as 8 polymorphs)	2.8/4.8	332/200	Excellent
	Li_2MnSiO_4		4.1/4.5	333/250	\
	Li_2CoSiO_4		4.2/5.0	325/100	\
Fluorophosphates	$Li(Na)VPO_4F$	Triclinic (space group $P\bar{1}$)	4.2	156/155	Excellent
	$Na_3V_2(PO_4)_2F_3$	Tetragonal (space group $P4_2/mnm$)	4.1	192/120	\
	$Li_5V(PO_4)_2F_3$	Layered monoclinic (space group $P2_1/c$)	4.1	170 (V^{3+}/ V^{4+}/ V^{5+}) redox couples)/70	\
	$Li(Na)_2FePO_4F$	Layered or stacked or 3D structure was	3.5	292/135	Good
	$Li(Na)_2MnPO_4F$		\	\	\
	$Li(Na)_2CoPO_4F$		5.0	287/120	\

	$Li(Na)_2NiPO_4F$	adopted depends on the alkali ion and transition metal ion	5.3	287₩(not determined)	\
Fluorosulphates	$LiFeSO_4F$	Triclinic (space group $P\bar{1}$)	3.6	151/135	\
	$LiMSO_4F$ (M = Co,Ni)	Triclinic (space group $P\bar{1}$)	\	\	\
	$LiMnSO_4F$	Monoclinic (space group $P2_1/c$)	\	\	\
Borates	$LiFeBO_3$	Monoclinic (space group $C2/c$)	3.0	220/200	\
	$LiCoBO_3$	Monoclinic (space group $C2/c$)	\	215\ (no data available)	\
	$LiMnBO_3$	Hexagonal (space group $P6$)	\	222/110	\

Table 1.2 Properties of some polyanion compounds [4]

1.2 Introduction of $LiFeBO_3$

1.2.1 Advantages and disadvantage of $LiFeBO_3$

Inspired by the successful development of $LiFePO_4$, the research for improved cathode materials has turned to the integration of other oxoanion systems with potentially larger energy densities. One such system is $LiFeBO_3$, where the higher charge/mass ratio of the BO_3^{3-} groups leads to a theoretical charge capacity of 220 mAh/g, about 30% larger than that of PO_4^{3-}-based $LiFePO_4$ [14]. $LiFeBO_3$ exhibits a larger reversible capacity of 200 mAh g^{-1} under moderate current density with the surprisingly small volume change of ca. 2%. The inherent activity of Li_xFeBO_3 is supported by *ab initio* calculations and indicates potential as an electrode material with no thermodynamic limitation for approaching a theoretical capacity of 220 mAh/g [15]. The electronic and ionic conductivity of LFeB are not well established, while the electrical conductivity has been reported as 1.5×10^{-4} S cm^{-1} [14, 16]. However, further researches of LFeB-based cathod materials are required to improve their electrochemical performances.

1.2.2 Structure of $LiFeBO_3$

Legagneur et al. first reported the electrochemical properties of $LiFeBO_3$ as cathode material in Li-ion batteries using experimental techniques. The crystal structures of $LiFeBO_3$ were determined from single-crystal data [4, 8, 17]. The three-dimensional $[FeBO_3]_n^{n-}$ framework is built up from FeO trigonal bipyramids and BO_3 groups (Figure 1.5). Each FeO bipyramid shares two 5 edges with adjacent bipyramids to form single chains running along the [-101] direction (Figure 1.6). The planar BO_3 groups link three chains via corner-sharing. Within this framework, the Li atoms occupy statistically two tetrahedral sites sharing a face. Such pairs of tetrahedra share edges to form chains running along the [001] direction. The Fe cation occupies statistically two close positions (Fe(1)–Fe(2) = 0.24(1) A) within the FeO bipyramid, above and below the central plane [17].

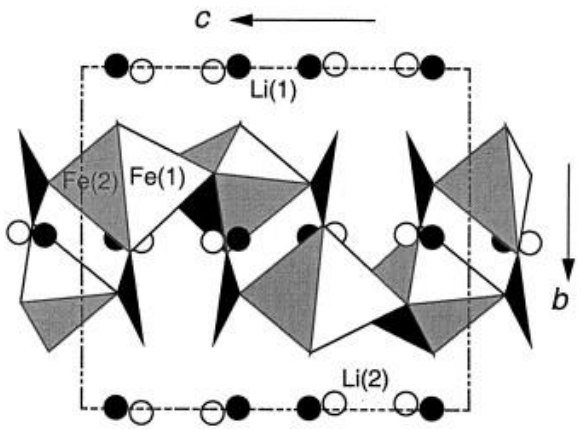

Figure 1.5 View of the LiFeBO structure along [100]* showing edge-sharing FeO_5, trigonal bipyramids (in grey), planar BO_3 groups (black triangles) and pairs of Li(1) (black circles) and Li(2) (open circles) sites (half occupied) [17].

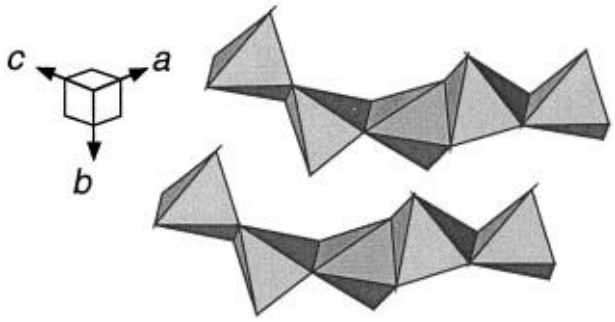

Figure 1.6 Perspective view of two chains of FeO_5 trigonal bipyramids running along [1 0 1] [17].

1.2.3 Synthesize method of $LiFeBO_3$

There are many kinds of methods to synthesize LFeB, such as conventional solid-state reaction at room temperature [18]. Then, Nanoporous composite of $LiFeBO_3$/C synthesized by applying the Pechini sol-gel technique using citric acid and ethylene glycol [19]. Furthermore, rod-like light grey transparent $LiFeBO_3$ single crystals were synthesized by solid-state reaction route and a porous framework containing many agglomerated small crystallites of $LiFeBO_3$ synthesized by self-combustion technique [20]. Also, nanostructured carbon-coated $LiFeBO_3$ synthesized by solution combustion [21]. And, nano-sized $LiFeBO_3$/C composite materials were synthesized by sol-gel method using citric acid as a carbon source [22]. However, $LiFeBO_3$ materials are sensitive to water and oxygen. Contact with a small amount of air at room temperature will seriously affect the material circulation of electrochemical performance. In order to avoid this shortcoming, the solid-state method is the best choice for synthesis of $LiFeBO_3$ [16, 22, 23].

1.2.4 Cation and anion substitution polyanion cathode material

Several reports have shown the effect of cation substitution in polyanion cathode such as $LiFePO_4$. The Cr doped $LiFePO_4$/C was successfully synthesized by the solid-state method and it was observed that the Cr doping facilitated the phase transformation during cycling and thus improved the rate performances of $LiFePO_4$/C [24]. Furthermore, the Ni-doped $LiFePO_4$/C nanocomposite was synthesized by a simple solid-state reaction and showed that the Ni doping attributed to the great enhancement of electronic conductivity, and the decrease in particle size distribution in the range of 20–60nm has improved the lithium-ion transition rate effectively [25]. In other work, minor doping of $LiFePO_4$/C compounds with Mn has shown a positive effect in enhancing the performance of $LiFePO_4$/C under extreme conditions [26].

Besides cation substitutions [24-26], anion substitution with species such as fluorine and iodine at the phosphate tetrahedral polyanion site in the olivine structure $LiMPO_4$ (M = Fe and Mn) has been considered to enhance electrical conductivity and electrochemical properties [27, 28]. Also, hybrid-structured $LiFe(PO_4)_{0.5}(BO_3)_{0.5}$ as a cathode material exhibits high specific discharge capacity [29, 30]. In this work, we have used fluorine anion as a substituent to improve the electrochemical properties of LFeB without carbon coating. $LiFeBO_{3-x}F_{2x}$ (LFeBF, x = 0, 0.05, 0.1, 0.2, 0.3, and 0.5) have been synthesized by solid-state

reaction method followed by high temperature treatment. The fine structure, morphology, and electrochemical properties of LFeBF have been investigated.

2. Experimental

2.1 Material synthesis

$LiFeBO_{3-x}F_{2x}$ (x = 0.00, 0.05, 0.10, 0.20, 0.30, 0.50) was prepared by solid-state method. $CH_3COOLi{\cdot}2H_2O$ (Junsei, ≥99%), $FeC_2O_4{\cdot}2H_2O$ (Junsei, ≥99%), H_3BO_3 (Kanto, ≥99.5%), and LiF (Wako, ≥98%) were used as the main precursor to synthesize $LiFeBO_{3-x}F_{2x}$. Stoichiometric amounts of the reactants were planetary milled with zirconia balls for 2 hr at 300 rpm in acetone reaction media, and the resulting precursor powder was dried in an oven at 80 °C for 12 hrs and grounded using a mortar and pestle. The fine precursor powder was purged to prevent oxidation in a tube furnace under pure argon gas for 5 hrs and sintered at 700 °C for 12 hrs.

2.2 Material characterization

X-ray diffraction (XRD, Rigaku Ultima IV, Germany) with Cu K_α radiation (λ = 1.5406 Å) was operated at 50 kV and 40 mA over the 2θ range between 15° and 80°. The 2θ scanning rate is 2° min^{-1} was used to identify the phases of the synthesized materials.

Ex-situ x-ray diffraction (XRD, Bruker D2 phase, Germany) was operated at 30 kV and 10 mA over the 2θ range between 10° and 80°. The 2θ scanning rate is 1° min^{-1} was used to identify cathode materials after first cycle. The measuring cathode material was directly on Al foil as the current collector. *Ex-situ* XRD was measuring in UNIST (Ulsan National Institute of Sciences and Technology).

^{7}Li magic angle spinning (MAS) nuclear magnetic resonance (NMR, Bruker Avance III 300, Germany) measurements were carried out at room temperature with a 7.04 T magnet. For the ^{7}Li MAS NMR experiments, a 2.5 mm MAS probe was used with a zirconia rotor at 116.64 MHz. The ^{7}Li NMR spectra were referenced to the external 1M LiCl. The Hahn-echo pulse sequences were used to observe the NMR signal and the sample spinning rate was 25 kHz. The ^{7}Li spectra were acquired with a 90° pulse length of 2.0 μs, repetition delay of 0.5 s, 1024 transients, and spectral width of 0.23 MHz.

Field emission scanning electron microscopy (FE-SEM, JEOL JSM-7610F, Japan) combined energy dispersive spectrometer (EDS, Oxford Instrument X-Max, England) was performed at 10 kV, 8 mm WD, and probe current of 5 nA. Synthesized material was prepared by spread on the surface of carbon tape and followed by Pt-coating, which was prepared by Sputter Coater 108auto (Cressington, England).

Laser induced breakdown spectroscopy (LIBS, J200 Tandem LA-LIBS Instrument, Applied Spectra, Inc.) was operated with delay time 0.2 μs, 100% laser power, 100 μm for spot size, and number of averaged spot is 100. LIBS was measuring in Hanyang University.

2.3 Electrochemical characterization

Cathode electrode was prepared by mixed active material (80 wt%), polyvinylidene fluoride (PVDF, Aldrich, Mw = 534,000, 10 wt%), and carbon black (Super P, 10 wt%) with some amount of n-methyl-2-pyrrolidone for zirconia planetary ball milling. The mixture-slurry was coated on aluminum foil and dried in a vacuum oven at 100 °C for 10 hr. Lithium metal foil was used as counter electrode, and non-aqueous 1.15 M $LiPF_6$ in ethylene carbonate/dimethyl carbonate/diethyl carbonate (3:4:3 v/v%) was used as electrolyte. Coin cell was assembled in the glove box under argon gas atmosphere used 2016 type coin cell. Charge-discharge properties were measured by galvanostatic automatic battery cycler (WonATech WBCS 3000, Korea). The cells for the rate test were cycled between 1.0 and 4.5 V vs. Li/Li^+ with a constant current-constant voltage (CC-CV) protocol in charging mode. The constant current rates at 0.05, 0.1, 0.2, 0.5, 1.0 and 2.0 C from 1.0 V to 4.5 V are used. Cyclic voltammetry (CV) at room temperature for all samples was performed at a scan rate of 0.05 mV s^{-1} over the voltage range of 1.0 - 4.5 V. Long cycle ability performed at 1 C for 51 cycles with voltage range 1.0 - 4.5 V. Another long cycle ability test performed at 0.05C for initial cycle, and 1 C for second cycle to 51st cycle with voltage range 1.0 - 4.5 V.

3. Results and discussion

3.1 X-ray diffraction

3.1.1 X-ray diffraction of $LiFeBO_3$

X-ray diffraction (XRD) patterns of $LiFeBO_3$ (LFeB) pristine is showed in **Figure 3.1** with rieatveld refinement using match software. Rieatveld refinement of XRD pattern from LFeB pristine material indicates the formation of single-crystalline monoclinic phase, which is well-matched with previous literature from *Legagneur et al.*[17], who the first one synthesized LFeB. From rieatveld refinement showed that sample of LFeB pristine has high purities.

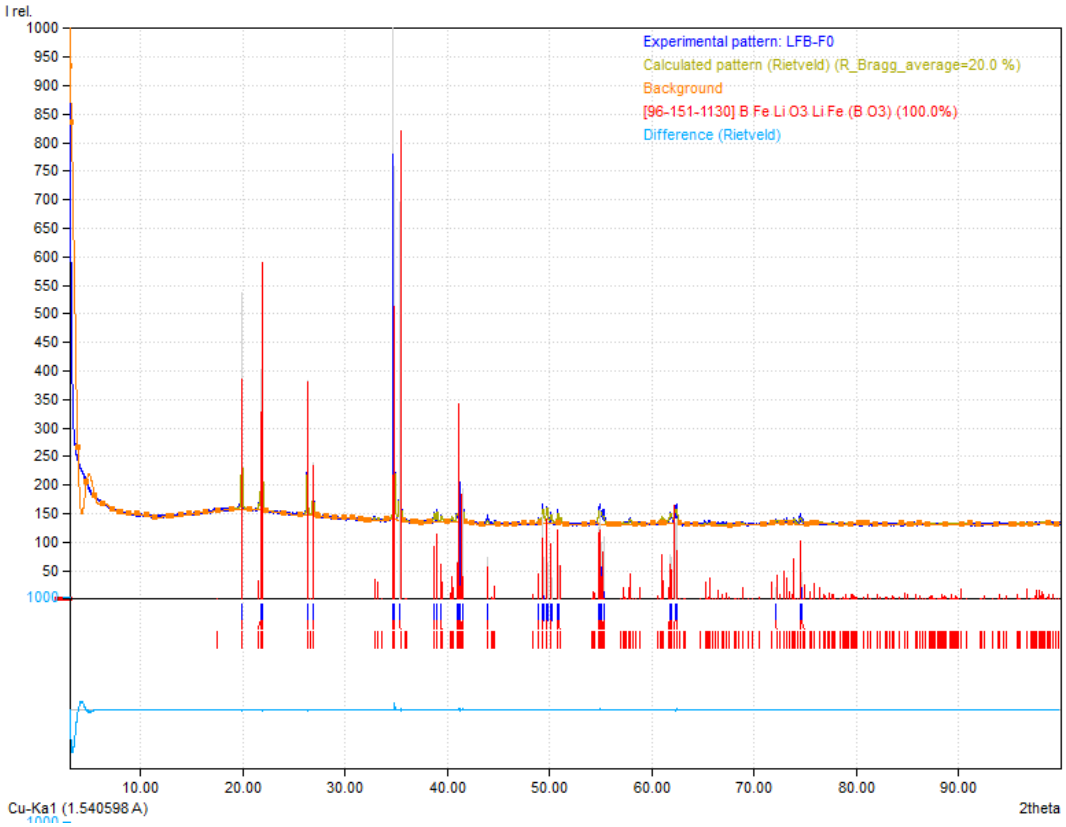

Figure 3.1 Rieatveld refinement result of the XRD pattern of $LiFeBO_3$.

3.1.2 X-ray diffraction of $LiFeBO_{3-x}F_{2x}$ (x = 0.05)

XRD patterns of the $LiFeBO_{3-x}F_{2x}$ (LFeBF, x = 0.05) are showed in **Figure 3.2**, with rieatveld refinement using match software. Rieatveld refinement of XRD pattern from LFeBF (x = 0.05) material indicates the small amount formation of single-crystalline monoclinic phase, which is matched with previous literature from *Legagneur et al.*[17]. Rieatveld refinement calculation showed that the sample was match with Fe_3BO_5 (vonsenite) and $LiBO_2$ with high percentage, more than LFeB. Based on rieatveld refinement calculation, with the fluorine substitution on LFeB (x = 0.05) can be effected to some amount of LFeB structure change to vonsenite and $LiBO_2$.

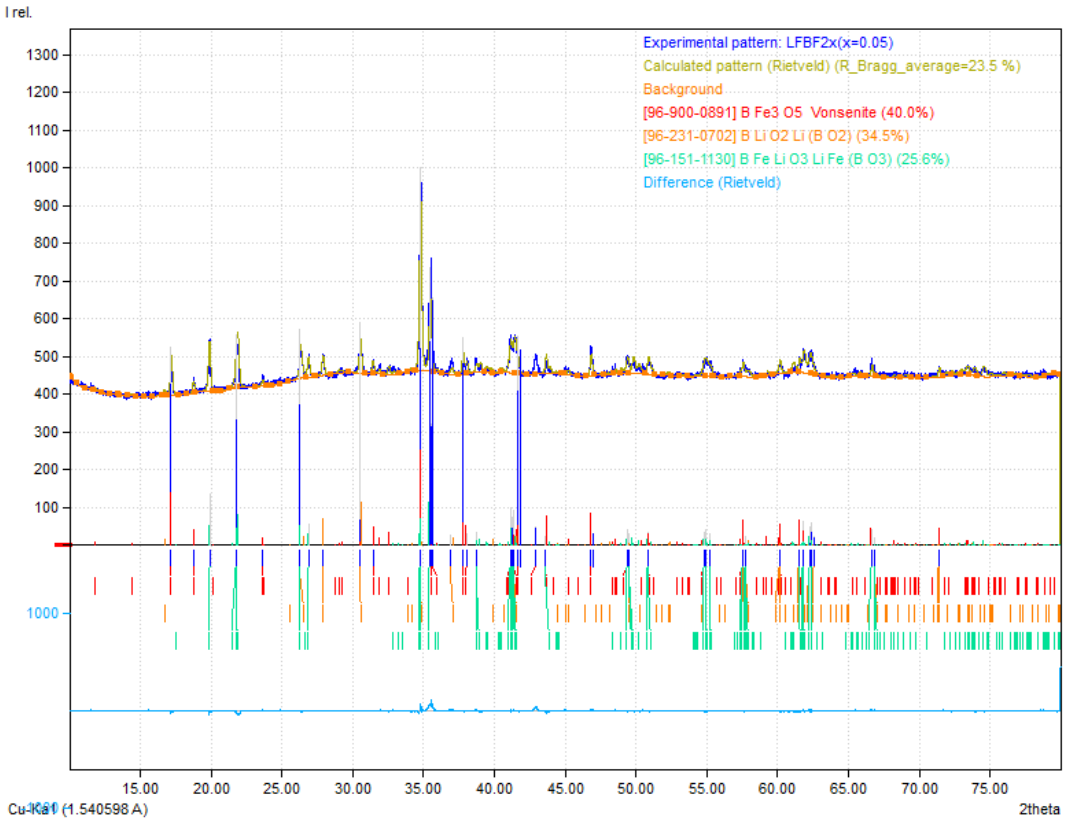

Figure 3.2 Rieatveld refinement result of the XRD pattern of $LiFeBO_{3-x}F_{2x}$ (x = 0.05).

3.1.3 X-ray diffraction of $LiFeBO_{3-x}F_{2x}$ (x = 0.1)

XRD patterns of the LFeBF (x = 0.1) are showed in **Figure 3.3**, with rieatveld refinement using match software. Rieatveld refinement of XRD pattern from LFeBF (x = 0.1) material indicates that the LFeB not found at the sample. Based on the rieatveld refinement, the sample was match with $LiBO_2$ and vonsenite as the major and small amount of LiF also observed.

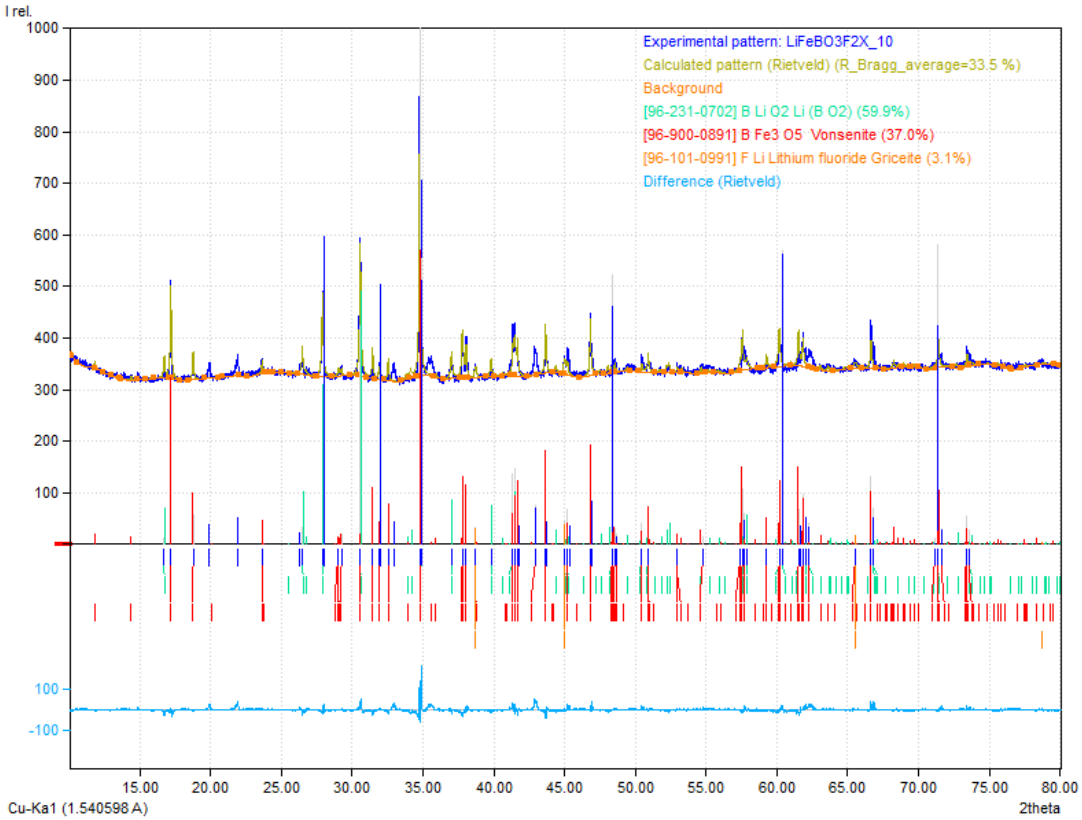

Figure 3.3 Rieatveld refinement result of the XRD pattern of $LiFeBO_{3-x}F_{2x}$ (x = 0.1).

3.1.4 X-ray diffraction of $LiFeBO_{3-x}F_{2x}$ (x = 0.2)

XRD patterns of the LFeBF (x = 0.2) are showed in **Figure 3.4**, with rieatveld refinement using match software. Rieatveld refinement of XRD pattern from LFeBF (x = 0.2) material indicates the same result with LFeBF (x = 0.1), that the LFeB was not found at the sample. Based on the rieatveld refinement, the sample was match with $LiBO_2$ and vonsenite as the major, and small amount of LiF also observed. Rieatveld refinement of XRD pattern from LFeBF (x = 0.2) compared LFeBF (x = 0.1) showed the percentage of $LiBO_2$ and vonsenite was decreased and the percentage of the LiF was increase.

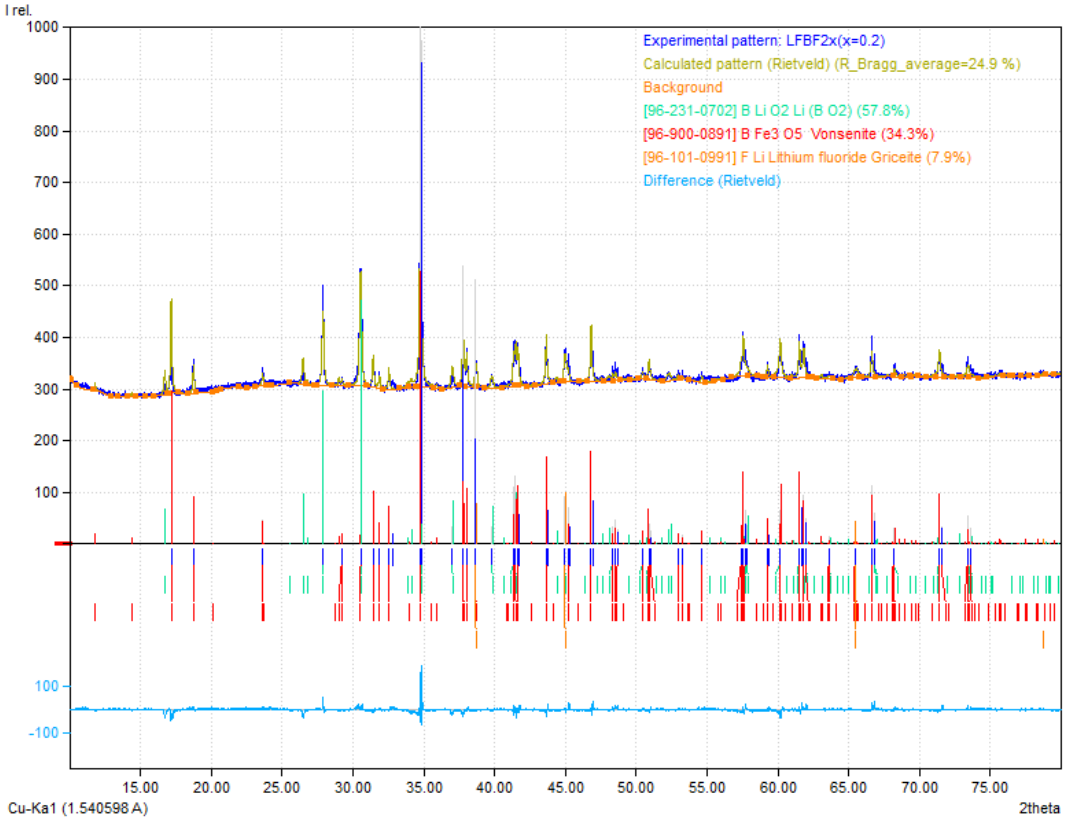

Figure 3.4 Rieatveld refinement result of the XRD pattern of $LiFeBO_{3-x}F_{2x}$ (x = 0.2).

3.1.5 X-ray diffraction of $LiFeBO_{3-x}F_{2x}$ (x = 0.3)

XRD patterns of the LFeBF (x = 0.3) are showed in **Figure 3.5**, with rieatveld refinement using match software. Rieatveld refinement of XRD pattern from LFeBF (x = 0.3), indicated that the LFeBF (x = 0.3) was match with vonsenite and LiF. The vonsenite was shows high percentage that match with the LFeBF (x = 0.3), and LiF was show low percentage match with LFeBF (x = 0.3). The LFeB pristine was not observed from LFeBF (x = 0.3).

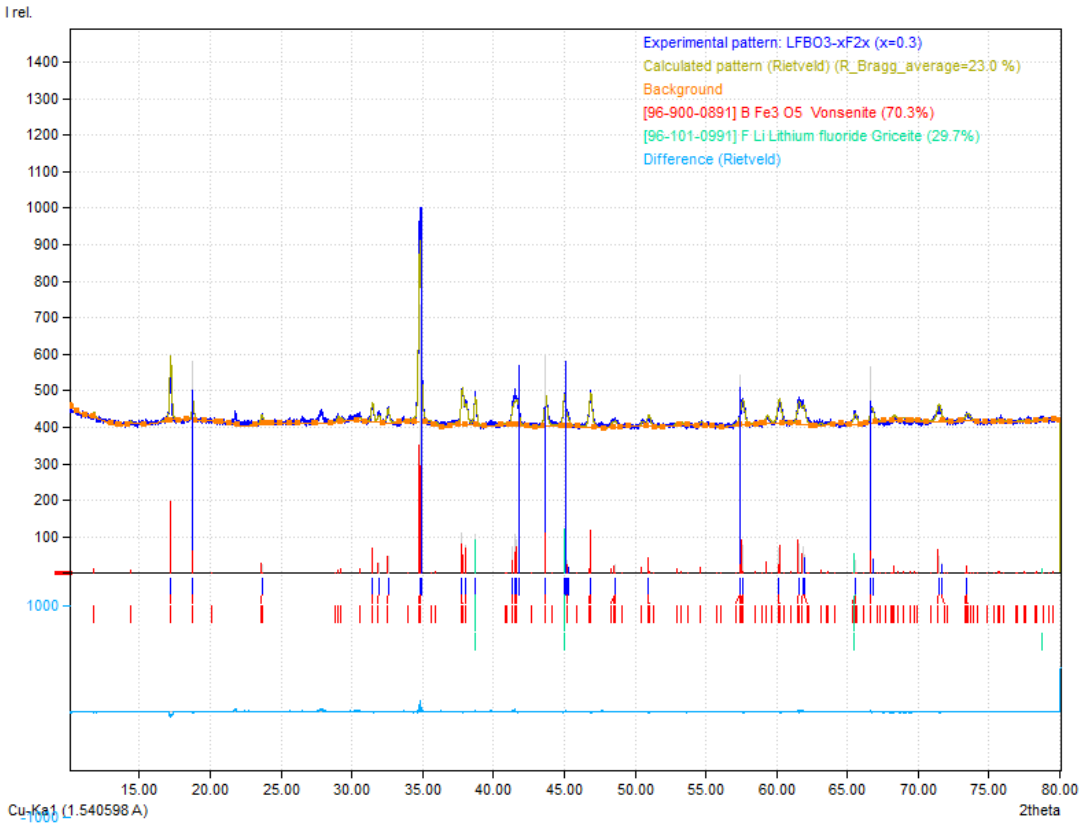

Figure 3.5 Rieatveld refinement result of the XRD pattern of $LiFeBO_{3-x}F_{2x}$ (x = 0.3).

3.1.6 X-ray diffraction of $LiFeBO_{3-x}F_{2x}$ (x = 0.5)

XRD patterns of the LFeBF (x = 0.5) are showed in **Figure 3.6**, with rieatveld refinement using match software. Rieatveld refinement of XRD pattern from LFeBF (x = 0.5), indicated that the LFeBF (x = 0.3) was match with vonsnite, $Li_2B_4O_7$, and LiF. Compared with LFeBF (x = 0.3), LFeBF (x = 0.5) also showed the major percentage of the vonsenite that match. In the LFeBF (x = 0.5), the percentage of vonsenite and LiF was decreased, while $Li_2B_4O_7$ was found in LFeBF (x = 0.5).

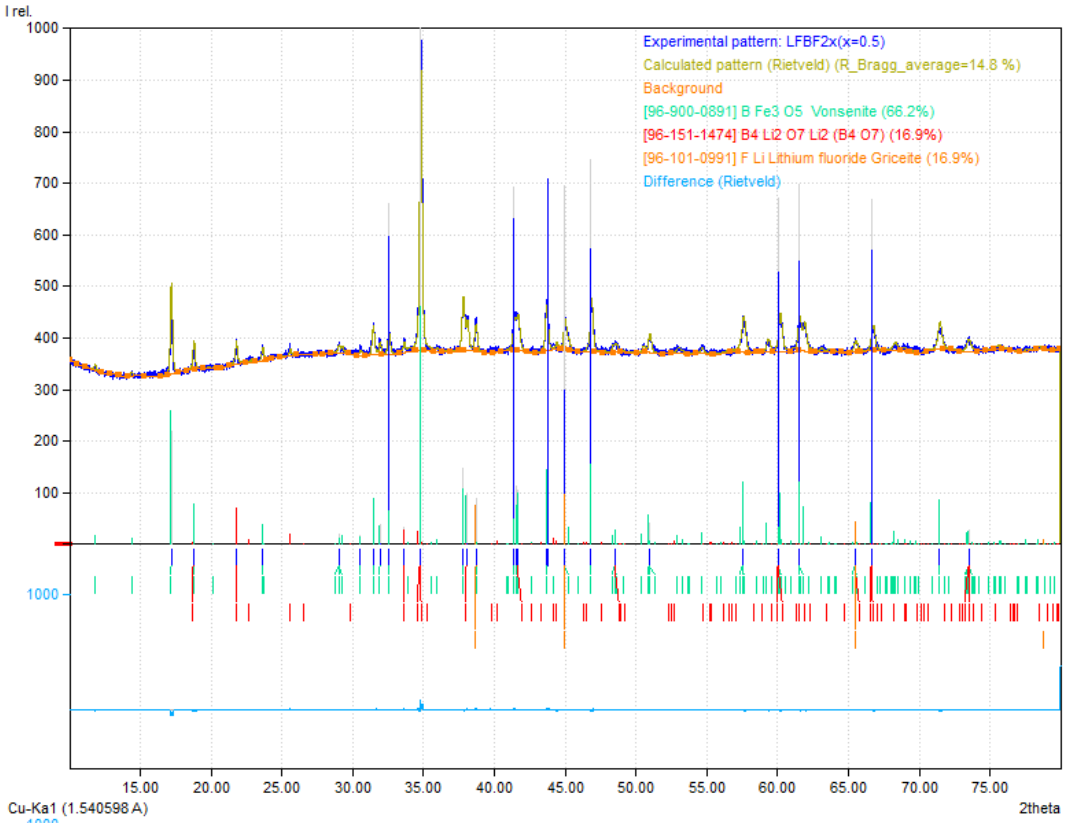

Figure 3.6 Rieatveld refinement result of the XRD pattern of $LiFeBO_{3-x}F_{2x}$ (x = 0.5).

X-ray diffraction (XRD) patterns of the LFeBF (x = 0, 0.05, 0.1, 0.2, 0.3, and 0.5) are showed in **Figure 3.7**. XRD pattern of $LiFeBO_3$ (LFeB) pristine material indicates the formation of single-crystalline monoclinic phase, which is well-matched with previous literature from *Legagneur et al.*[17], who synthesized LFeB as cathode material for the first time. XRD patterns of LFeBF illustrate an increase in vonsenite ($2FeO{\cdot}FeBO_3$) structure with increasing fluorine substitution ratio compared to that of monoclinic LFeB [31, 32]. Based on previous researches about monoclinic LFeB, vonsenite phase as an impurity has been obtained in synthesizing LFeB [15, 20, 31, 33, 34]. Therefore, the structural change from monoclinic to vonsenite is potentially high and both structures are very comparable. The obtained vonsenite structure of LFeBF with fluorine is supposedly $(FeO{\cdot}LiF){\cdot}FeBO_3$ based on previous reports [29, 31]. Besides vonsenite, XRD patterns shows the presence of impurities such as $LiBO_2$ in LFeBF (x = 0.05, 0.1, 0.2, and 0.3) and $Li_2(B_4O_7)$ in LFeBF (x = 0.5) . $LiBO_2$ and $Li_2(B_4O_7)$ can be found as interaction between Li and B-O bond in structure of vonsenite. LiF phase is also found from LFeBF (x = 0.1, 0.2, 0.3, and 0.5) as a minor phase of vonsenite $(FeO{\cdot}LiF){\cdot}FeBO_3$.

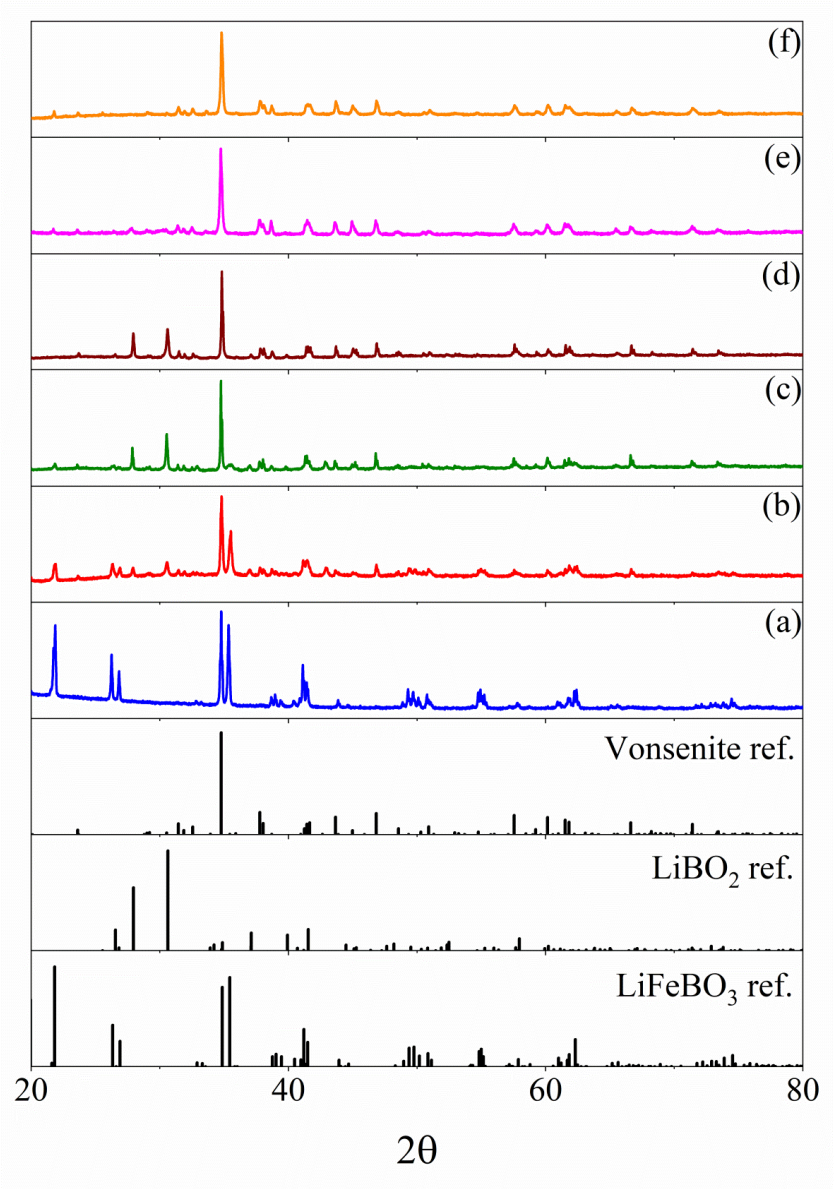

Figure 3.7 XRD patterns of $LiFeBO_{3-x}F_{2x}$ for x = (a) 0, (b) 0.05, (c) 0.1, (d) 0.2, (e) 0.3, and (f) 0.5 compared with vonsenite (Fe_3BO_5), $LiBO_2$, and $LiFeBO_3$ as references.

3.2 ^{7}Li magic angle spinning nuclear magnetic resonance spectroscopy

^{7}Li magic angle spinning (MAS) nuclear magnetic resonance (NMR) spectra of LFeBF are shown in **Figure 3.8**. The isotropic peak of ^{7}Li spectra is indicated with the dashed line and spinning sidebands manifolds with asterisks. The compounds LFeBF (x = 0 and 0.05) have an isotropic shift of -230 ppm and this large shift is caused by through-bond hyperfine interaction between the paramagnetic Fe^{2+} and Li^{+} through the intervening oxygen atoms [34, 35]. This chemical shift is well understood when the Li^{+} ions are surrounded by trigonal bipyramidal $FeBO_3$ in monoclinic structure [17]. Spinning sidebands for all samples are arising in every MAS rate due to the unpaired electrons of Fe^{2+}. The isotropic peak of LFeBF (x = 0.1, 0.2, 0.3, and 0.5) with high fluorine substitution ratio is, however, shifted downfield at around 0 ppm due to Li^{+} ions surrounded by octahedral Fe_2BO_3 in vonsenite [36]. As shown in the supplementary information of ^{11}B MAS NMR (Fig. S1), isotropic peak is shifted downfield from around 750 ppm for LFeB to around 1,000 ppm for LFeBF (x = 0.3) due to the structural change from monoclinic to vonsenite. Boron atoms also have through-bond hyperfine interaction with the paramagnetic Fe^{2+} ions via oxygen atoms, which can explain the downfield shift in vonsenite phase, in which one boron atom is surrounded by two Fe^{2+} ions, while in monoclinic phase it is surrounded by one a Fe^{2+} ion. This NMR peak shift to downfield by structural change of LFeBF is well agreed with XRD results.

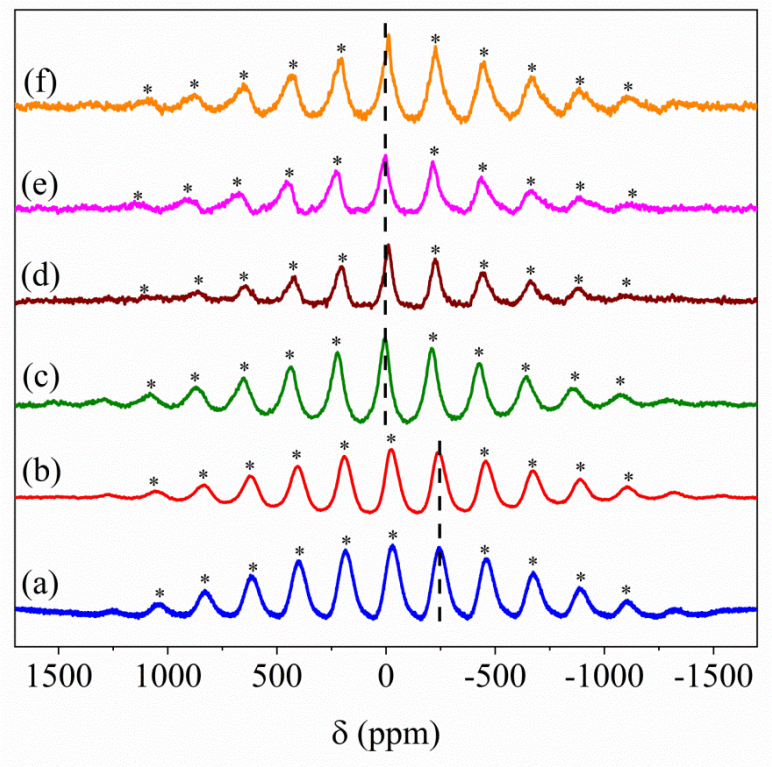

Figure 3.8 ^{7}Li MAS NMR spectra of $LiFeBO_{3-x}F_{2x}$ for x = (a) 0, (b) 0.05, (c) 0.1, (d) 0.2, (e) 0.3, and (f) 0.5.

3.3 Field emission scanning electron microscopy (FE-SEM) and energy dispersive x-ray spectroscopy

3.3.1 Field emission scanning electron microscopy (FE-SEM)

The morphology of synthesized LFeBF has been observed by field emission scanning electron microscopy (FE-SEM) as shown in **Figure 3.9**. In **Figure 3.9(a)**, LFeB pristine shows the particle size distribution around 1~3 μm. SEM images of LFeBF (x = 0.05, 0.1, and 0.2) show that the particle size has decreased due to the fluorine substitution, as shown in **Figure 3.3(b-d)**. On the other hand, SEM images of LFeBF (x = 0.3 and 0.5), illustrates also a decrease in size accompanied by the transformation into rod-shaped morphology, as shown in **Figure 3.3(e and f)**.

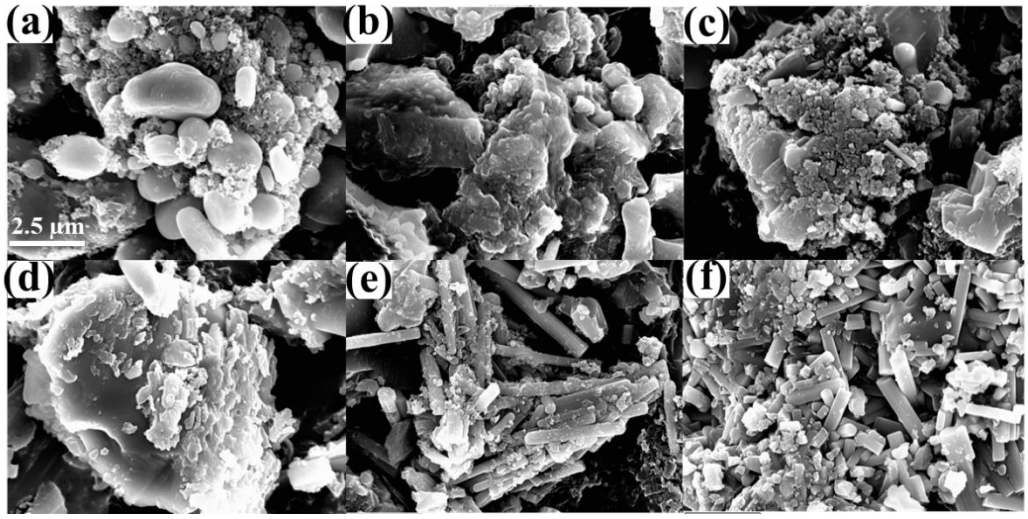

Figure 3.9 SEM images of $LiFeBO_{3-x}F_{2x}$ for x = (a) 0, (b) 0.05, (c) 0.1, (d) 0.2, (e) 0.3, and (f) 0.5.

3.3.2 Energy dispersive x-ray spectroscopy

Energy dispersive x-ray (EDX) spectra of LFeBF (x = 0, 0.05, 0.1, 0.2, 0.3, and 0.5) was showed in **Figure 3.10-3.15**. The EDX maps of LFeB pristine confirmed the good distribution of Fe, B, and O elements, see **Figure 3.10**. The EDX maps of LFeBF (x = 0.05, 0.1, 0.2, 0.3, and 0.5), was confirmed that all element like Li, Fe, B, and O was well distributed, including the substituted fluorine, see **Figure 3.11-3.15**.

.

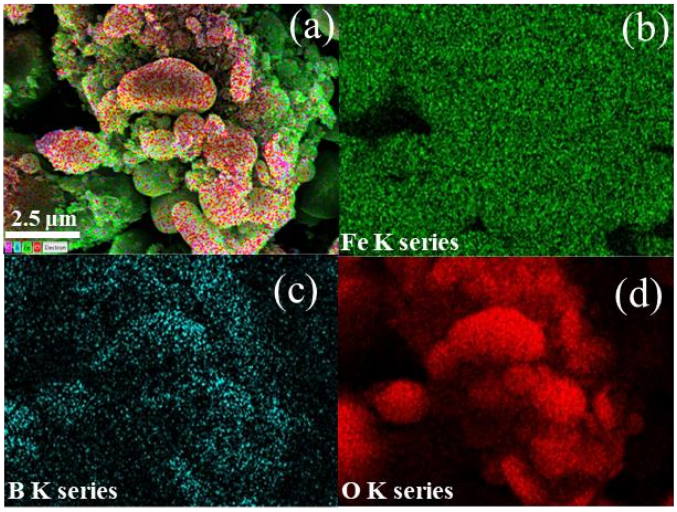

Figure 3.10 EDX element maps of $LiFeBO_{3-x}F_{2x}$ (x = 0) in the (a) SEM image for (b) Fe, (c) B, and (d) O.

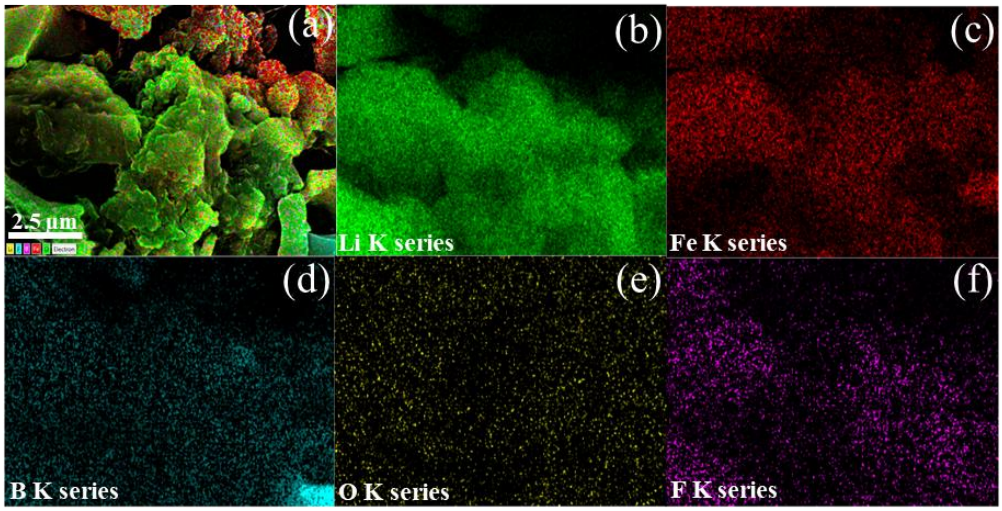

Figure 3.11 EDX element maps of $LiFeBO_{3-x}F_{2x}$ (x = 0.05) in the (a) SEM image for (b) Li, (c) Fe, (d) B, (e) O, and (f) F.

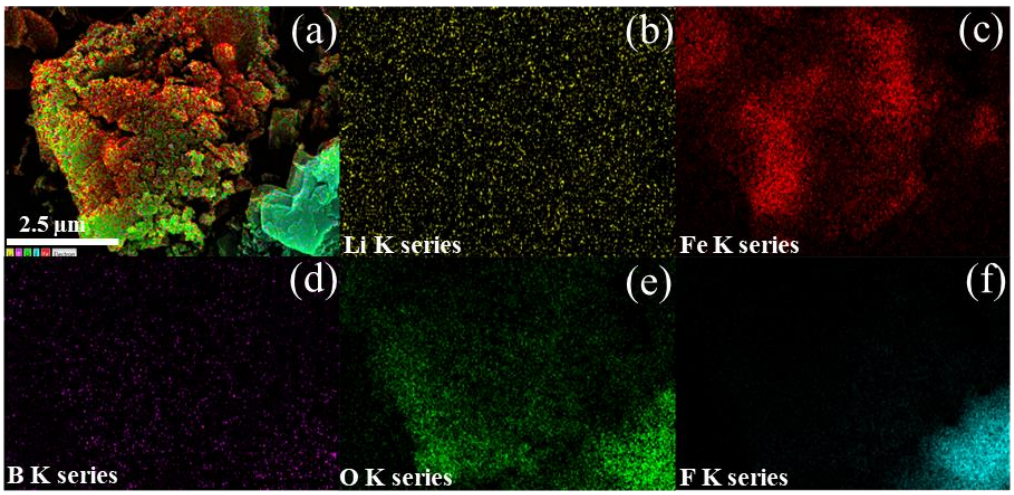

Figure 3.12 EDX element maps of $LiFeBO_{3-x}F_{2x}$ (x = 0.1) in the (a) SEM image for (b) Li, (c) Fe, (d) B, (e) O, and (f) F.

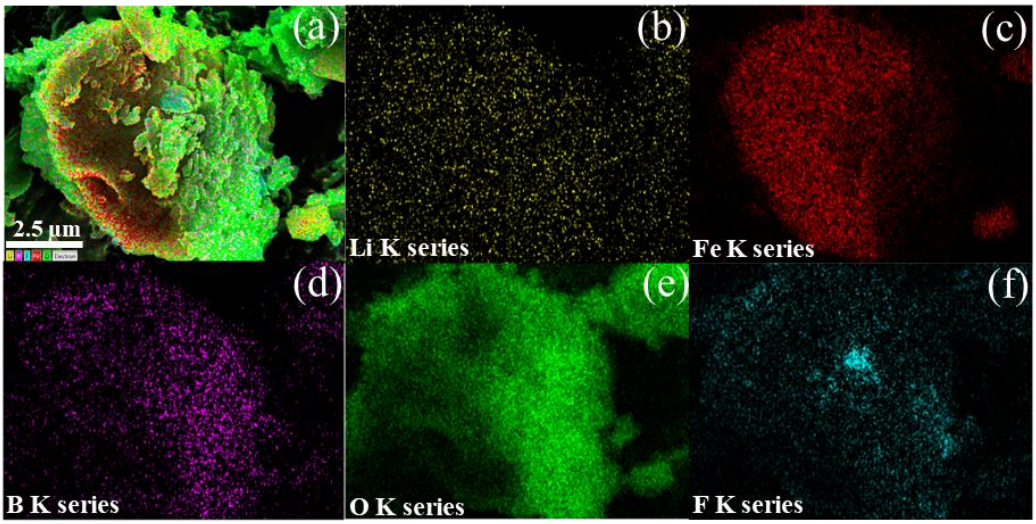

Figure 3.13 EDX element maps of $LiFeBO_{3-x}F_{2x}$ (x = 0.2) in the (a) SEM image for (b) Li, (c) Fe, (d) B, (e) O, and (f) F.

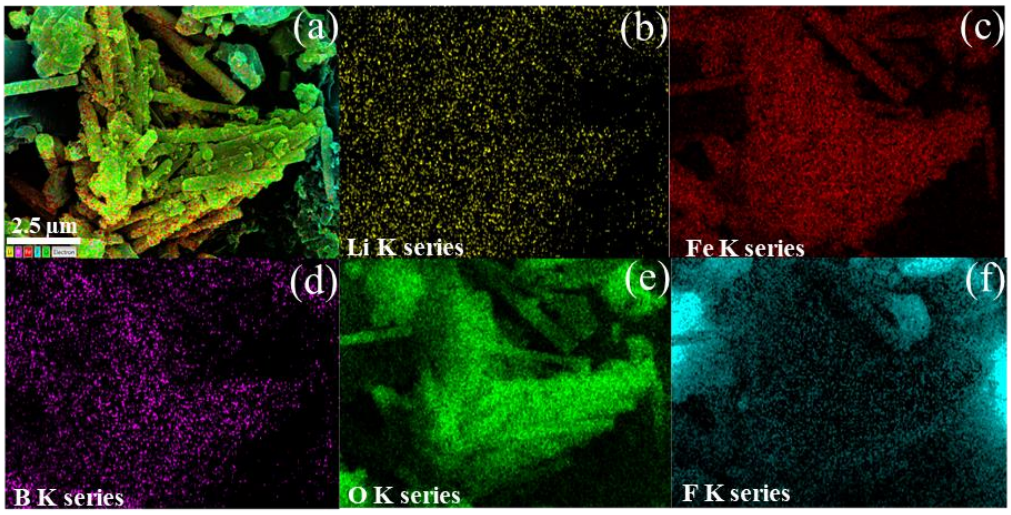

Figure 3.14 EDX element maps of $LiFeBO_{3-x}F_{2x}$ (x = 0.3) in the (a) SEM image for (b) Li, (c) Fe, (d) B, (e) O, and (f) F.

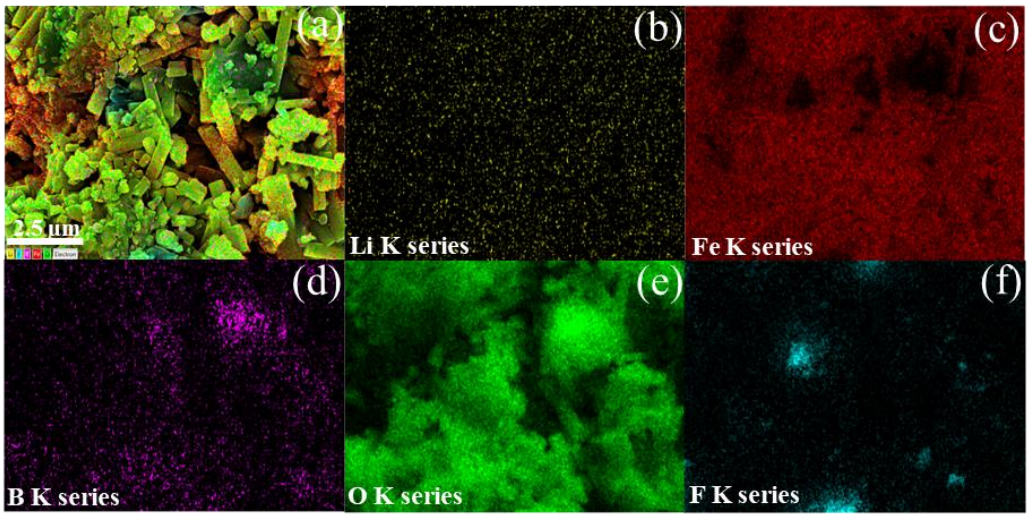

Figure 3.15 EDX element maps of $LiFeBO_{3-x}F_{2x}$ (x = 0.5) in the (a) SEM image for (b) Li, (c) Fe, (d) B, (e) O, and (f) F.

3.4 Laser induced breakdown spectroscopy

Laser induced breakdown spectroscopy (LIBS) spectra of LFeBF (x = 0, 0.05, 0.1, 0.2, 0.3, and 0.5) was showed in **Figure 3.16** and **Figure 3.17** for each element, respectively. The magnified peak of Li was showed in **Figure 3.16(a)**, the Li peak was observed as single peak around 812.5 nm. The magnified peak of Fe was showed in **Figure 3.16(b)**, the Fe peak was observed as multiple peak around 486 - 496 nm. The magnified peak of B was showed in **Figure 3.16(c)**, the B peak was observed as single peak around 345.1 nm. The magnified peak of O was showed in **Figure 3.16(d)**, the O peak was observed as single peak around 777.4 nm.

The magnified peak of F was showed in **Figure 3.17 (a)**, the F peak was observed as single peak around 685.55 nm. **Figure 3.17(b)** showed the calibration curve for doping amount of F in LFeBF (x = 0, 0.05, 0.1, 0.2, 0.3, and 0.5) between amount of F doped (x = 0, 0.05, 0.1, 0.2, 0.3, and 0.5) with the peak area of F element that observed. The calibration curve was showed the high linearity around 0.9757.

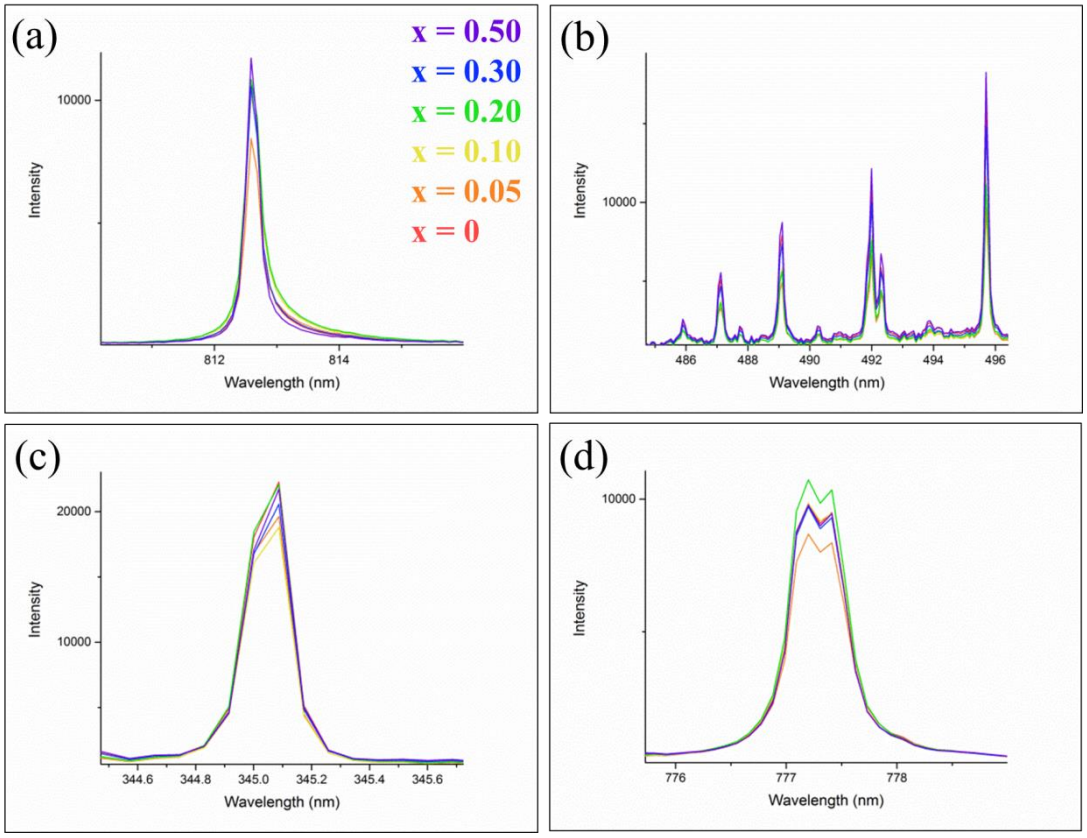

Figure 3.16 Magnified peaks of (a) Li, (b) Fe, (c) B and (d) O on the LIBS spectrum.

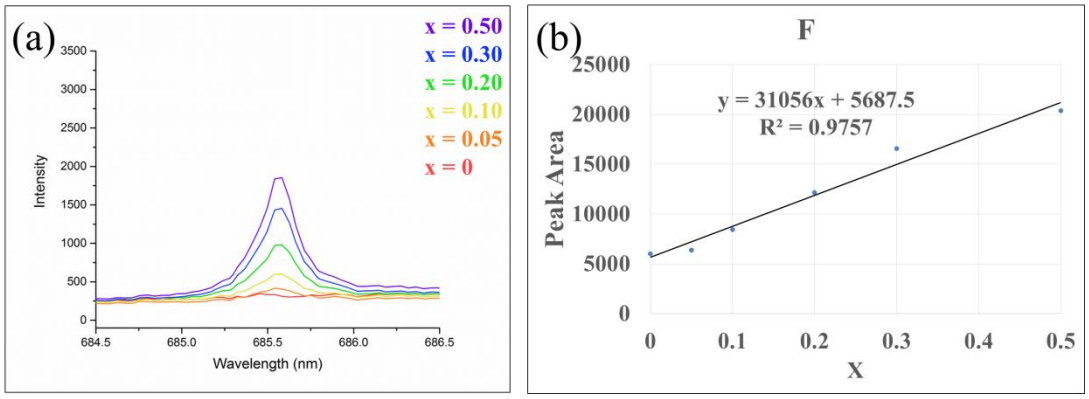

Figure 3.17 Magnified peaks of (a) F and (d) calibration curve for doping amount of F in $LiFeBO_{3-x}F_{2x}$.

3.5 Electrochemical properties

3.5.1 Rate performances

The electrochemical rate performances of LFeBF are shown in **Figure 3.18** with a voltage range of 1.0 – 4.5 V during charge and discharge performance depending on various C-rate from 0.05 to 2 C. **Figure 3.18** shows that the fluorine substitution in oxygen site in LFeB influence to increase the discharge capacity at all C-rates. LFeBF (x = 0, 0.05, 0.1, 0.2, 0.3, and 0.5) have shown an initial discharge capacity of 73.43, 228.20, 343.76, 382.31, 363.98 and 345.50 mAh g^{-1} at 0.05 C, respectively. Although, LFeBF (x = 0.2) shows highest discharge capacity at the initial cycle in 0.05 C rate, LFeBF (x = 0.3) shows the highest at the second cycle. The discharge capacities of all fluorine substituted LFeBF (x = 0.05, 0.1, 0.2, 0.3, and 0.5) exceeds the theoretical capacity of LFeB (220 mAh g^{-1}) at 0.05 C rate, but in the second cycle performance, their discharge capacities are rapidly stabilized down to 133.98, 202.61, 225.72, 254.66, and 251.216 mAh g^{-1}, respectively, at 0.05 C rate. LFeBF (x = 0.3) shows the highest discharge capacities and stability in all C-rates after the first cycle.

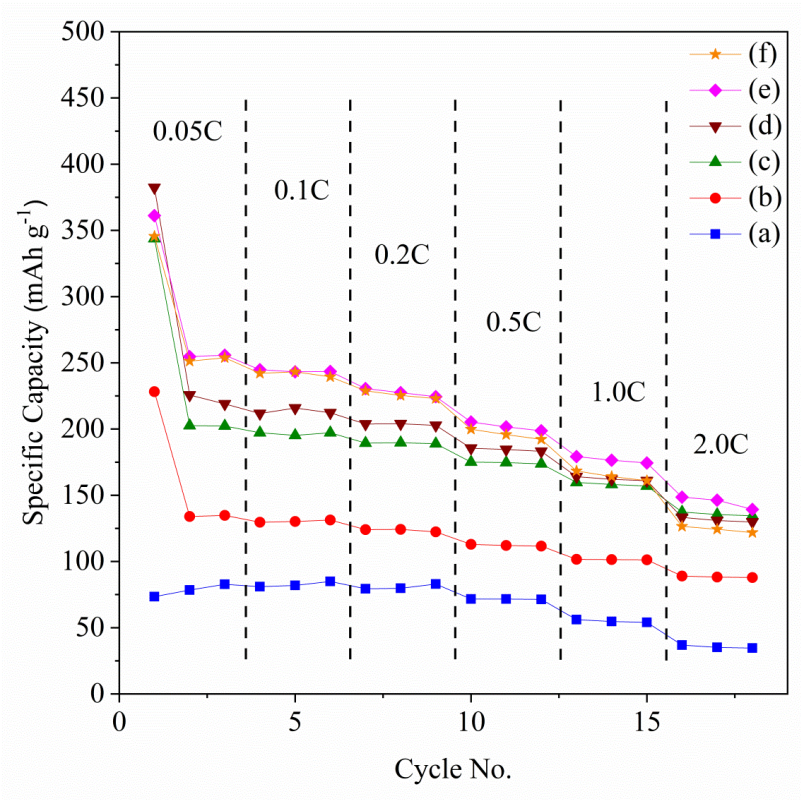

Figure 3.18 The rate performances of $LiFeBO_{3-x}F_{2x}$ for x = (a) 0, (b) 0.05, (c) 0.1, (d) 0.2, (e) 0.3, and (f) 0.5.

3.5.2 Electrochemical behavior of $LiFeBO_{3-x}F_{2x}$

The electrochemical performance of prepared LFeBF composites was investigated via galvanostatic charging/discharging in Li coin cells and the initial and second charge/discharge curves are shown in **Figure 3.19** and **Figure 3.20**. It is worthy to note that charge/discharge curves have remarkably changed and stabilized after the initial cycle. The initial discharge curve shows the plateau around 1.1 V, and that of second cycle around 1.6 V. Electrochemical properties of LFeBF show the improvement of the electrochemical properties by fluorine substitution at oxygen site in LFeB with structural change from monoclinic to vonsenite.

At the initial cycle, between charge and discharge curve shows the big different capacity, the charge curve show lower capacity. At the initial charge shows the short curve due to high open circuit voltage (OCV) before the measurement. The fluorine substitutions LFeB observed can be effected to the OCV of cell battery, where the fluorine substitutions increased the OCV cell battery. At the second cycle, the charge curve shows

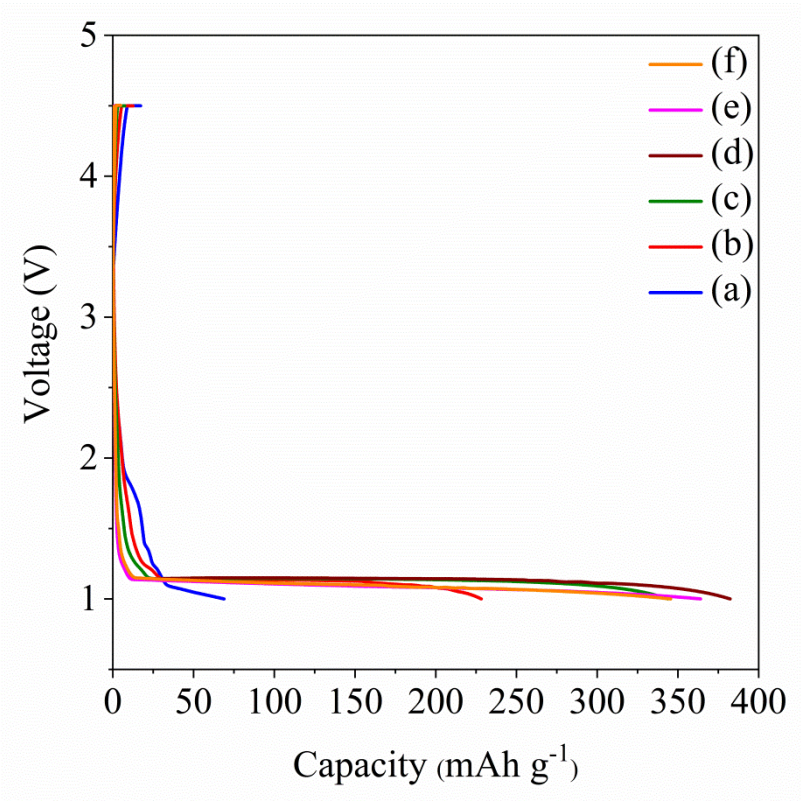

Figure 3.19 Initial cycle of charge/discharge curves of $LiFeBO_{3-x}F_{2x}$ for x = (a) 0, (b) 0.05, (c) 0.1, (d) 0.2, (e) 0.3, and (f) 0.5.

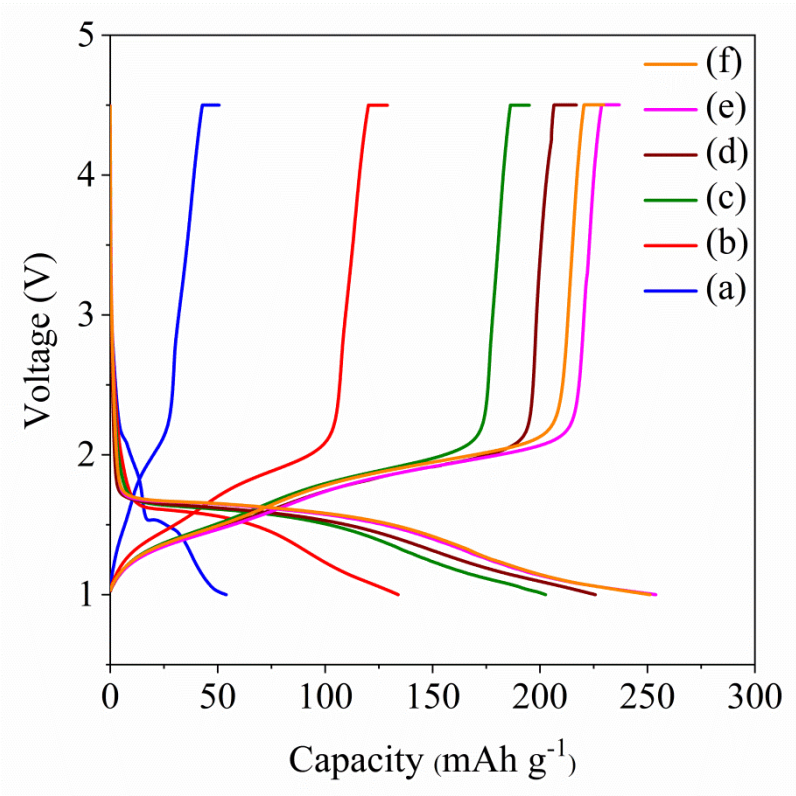

Figure 3.20 Second cycle of charge/discharge curves of $LiFeBO_{3-x}F_{2x}$ for x = (a) 0, (b) 0.05, (c) 0.1, (d) 0.2, (e) 0.3, and (f) 0.5.

3.5.3 Cyclic voltammetry properties of $LiFeBO_{3-x}F_{2x}$

The cyclic voltammetry (CV) curve of LFeBF (x = 0, 0.05, 0.1, 0.2, 0.3, and 0.5) are shown in **Figure 3.21 – Figure 3.26** with 0.05 mV s^{-1} of scan rate in voltage range of 1 – 4.5 V. The CV curve of LFeBF (x = 0) bare are shown several oxidation and reduction peak as shows in **Figure 3.21**. At initial cycle, LFeBF (x = 0) shows one main oxidation peak around 2 V and two small oxidation peak around 1.5 and 3 V, and for reduction peak was observed around 1.2, 1.4, 1.7, 1.9, and 2.3 V. For second cycle and forward, LFeBF (x = 0) shows the same trend of oxidation peak as initial cycle, with a small shifted to positive potential. However, the reduction peak of second cycle and forward, are shown different peak with two main peaks around 1.4 and 1.5 V, and two smalls peak around 1.9 and 2.1 V.

The CV curve of LFeBF (x = 0.05, 0.1, 0.2, 0.3, and 0.5) are displayed in **Figure 3.22 – Figure 3.26** and shows the same trends even different amount of fluorine substitution. The oxidation peaks are observed around 1.5 and 2 V, and the intensity of oxidation peaks are increased with number of cycle. At initial cycle, the reduction peaks of LFeBF (x = 0.05) are shown two peaks, small peak around 1.5 V and high peak around 1 V. For the second cycle and forward, the intensity of reduction peak around 1 V is decrease and reduction peak around 1.5 is increase. In different, initial cycle of LFeBF (x = 0.1, 0.2, 0.3, and 0.5) are shown single peak of reduction around 1 V, at second cycle and forward the

properties of reduction peaks are change become two peaks around 1 and 1.5 V. During cycle number increase, the intensity of reduction peak around 1 V is decreased, otherwise, the reduction peak around 1.5 is increased.

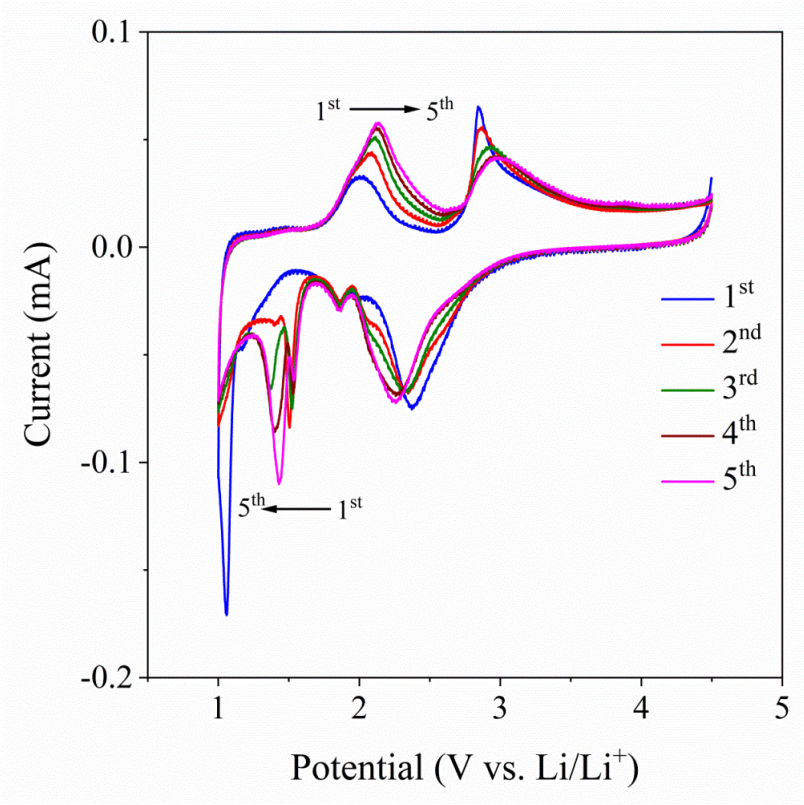

Figure 3.21 Cyclic voltammetry curves of $LiFeBO_{3-x}F_{2x}$ for x = 0.

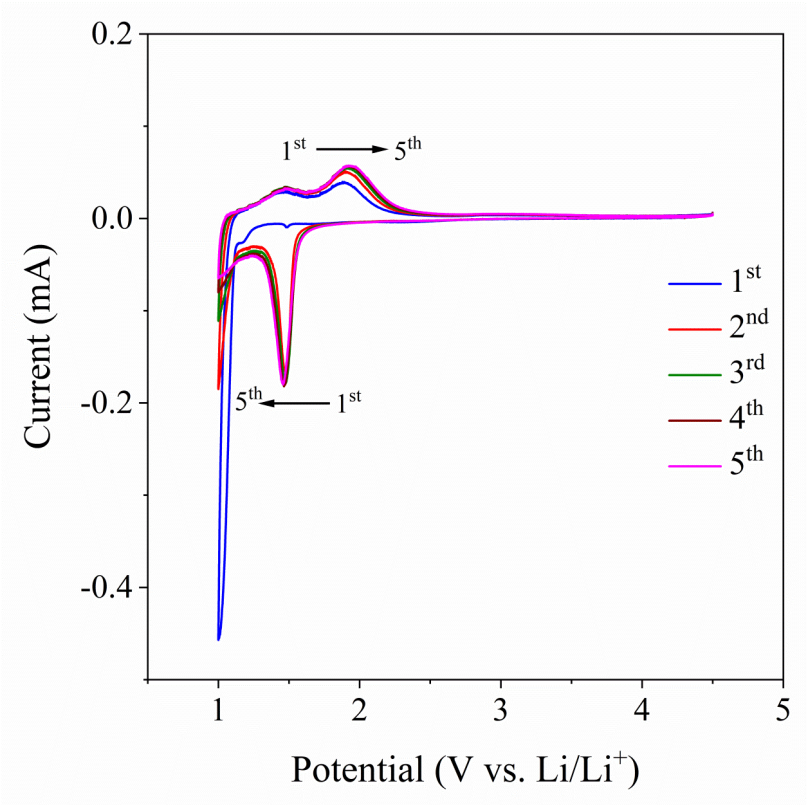

Figure 3.22 Cyclic voltammetry curves of $LiFeBO_{3-x}F_{2x}$ for x = 0.05.

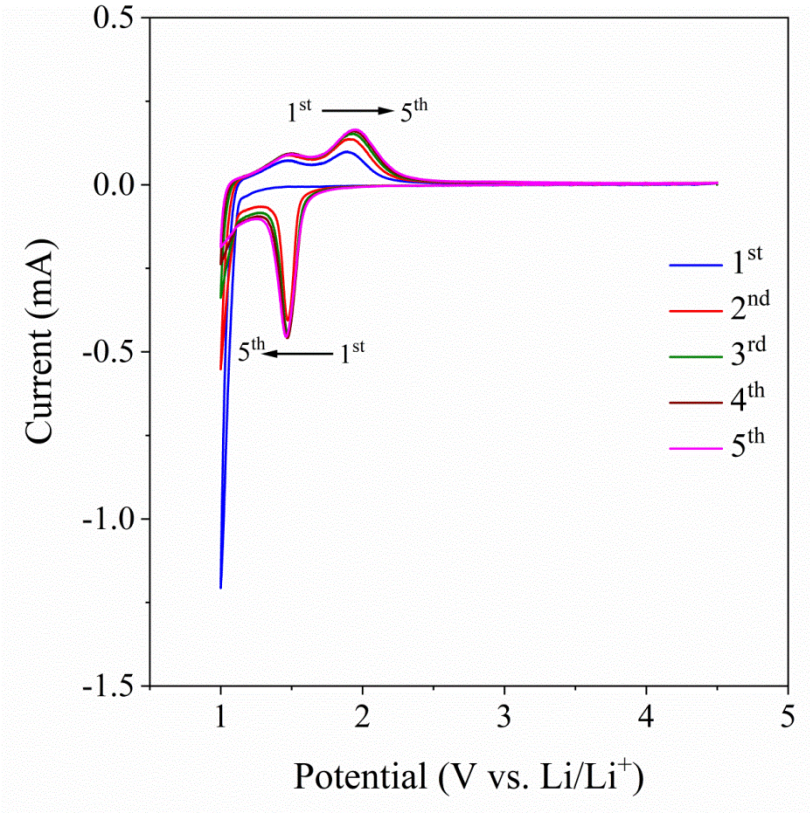

Figure 3.23 Cyclic voltammetry curves of $LiFeBO_{3-x}F_{2x}$ for x = 0.1.

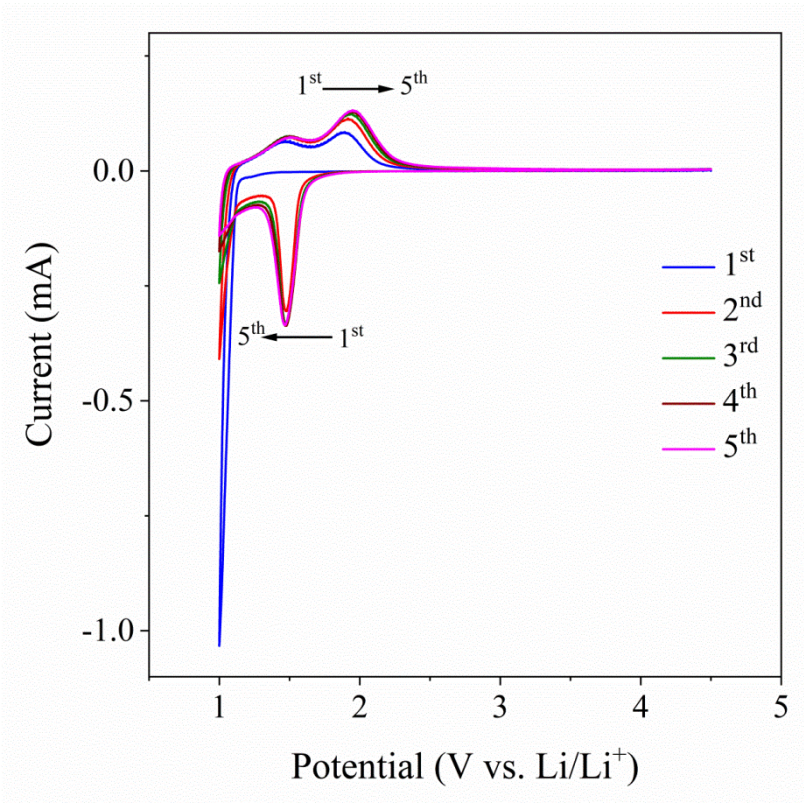

Figure 3.24 Cyclic voltammetry curves of $LiFeBO_{3-x}F_{2x}$ for x = 0.2.

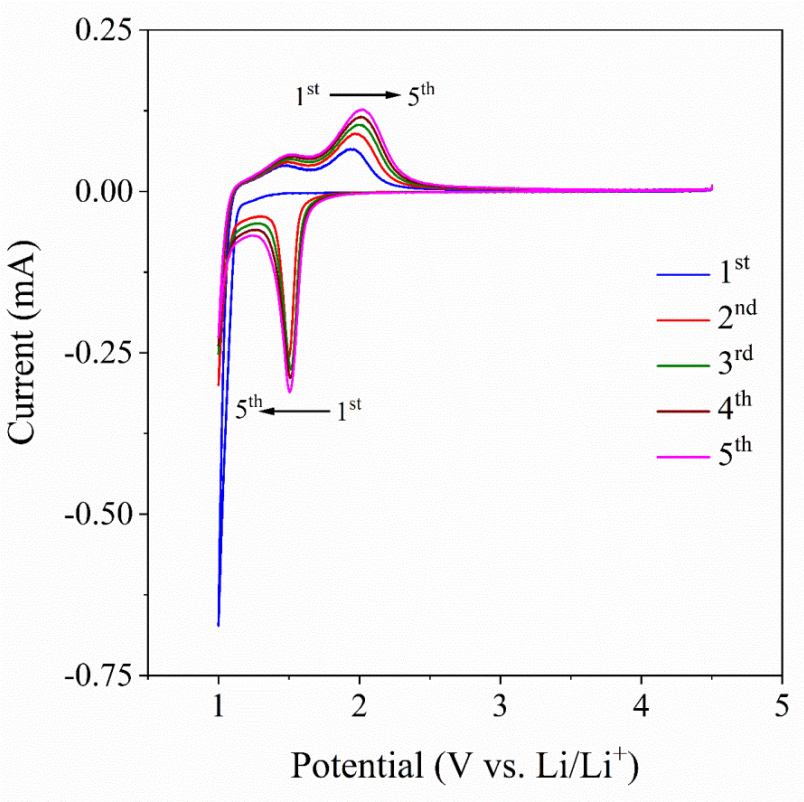

Figure 3.25 Cyclic voltammetry curves of $LiFeBO_{3-x}F_{2x}$ for x = 0.3.

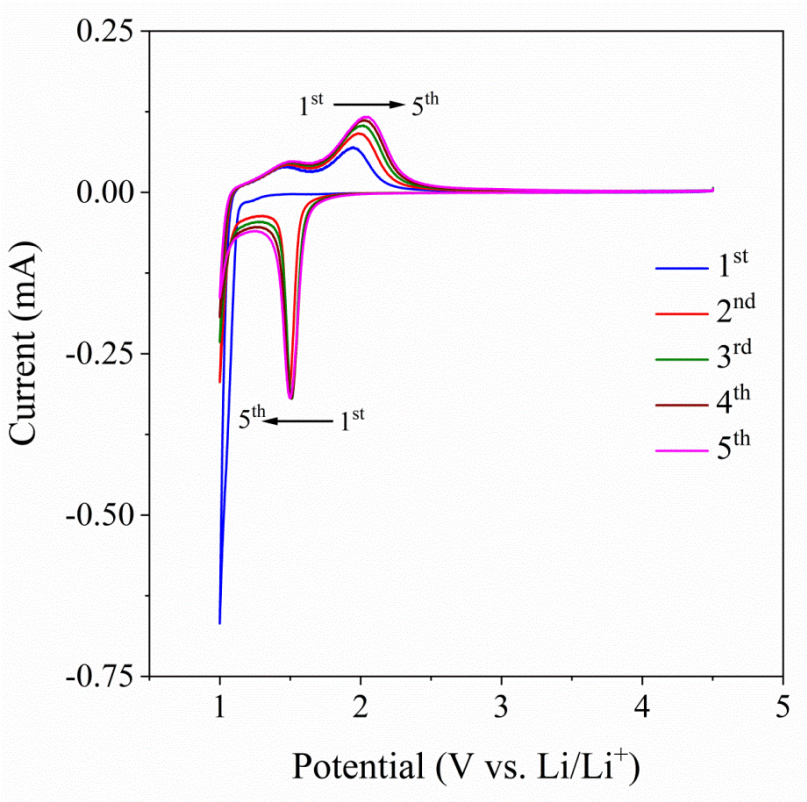

Figure 3.26 Cyclic voltammetry curves of $LiFeBO_{3-x}F_{2x}$ for x = 0.5.

3.5.4 Long cycle performance of $LiFeBO_{3-x}F_{2x}$

Long cycle ability of LFeBF (x = 0, 0.05, 0.1, 0.2, 0.3, and 0.5) are shown in **Figure 3.27,** performed with voltage range 1.0 – 4.5 V at 1 C rate. Long cycle performance shows that the fluorine substitution in oxygen site in LFeB influence to increase the discharge capacity. LFeBF (x = 0, 0.05, 0.1, 0.2, 0.3, and 0.5) are shown the initial discharge capacity of 47.1, 149.69, 235.20, 280.83, 130.17 and 263.88 mAh g^{-1} at 1 C, respectively. In the second cycle performance, discharge capacities of them are rapidly stabilized down to 46.64, 94.01, 146.11, 161.23, 95.72 and 181.76 mAh g^{-1} at 1 C rate, respectively. LFeBF (x = 0.5) shows the highest discharge capacities at the second cycle but the stability is rapidly decrease, it shows at the end of 51st cycle, the discharge capacity of LFeBF (x = 0.5) shows below LFeBF (x = 0.1). In different, LFeBF (x = 0.2) shows highest discharge capacity at the initial cycle for 1 C rate performance, and highest stability during 51 cycles working. Different with variation of C rate performance that LFeBF (x = 0.3) shows the highest performance during charge and discharge, in long cycle performance at 1 C, LFeBF (x = 0.3) shows low performance below LFeBF (x = 0.1).

Figure 3.38 shown long cycle performance with initial cycle at 0.05 C and continue working at 1 C for second cycle until 51st cycle. This work observed that LFeBF (x = 0.3) shows the highest performance with higher discharge capacity and higher stability after initial cycle at low C-rate. LFeBF (x = 0.3) shows the

good performance after treated in low cycle at initial cycle. The effect of low C-rate treated on LFeBF (x = 0.3) material to increase the electrochemical performance are under studying.

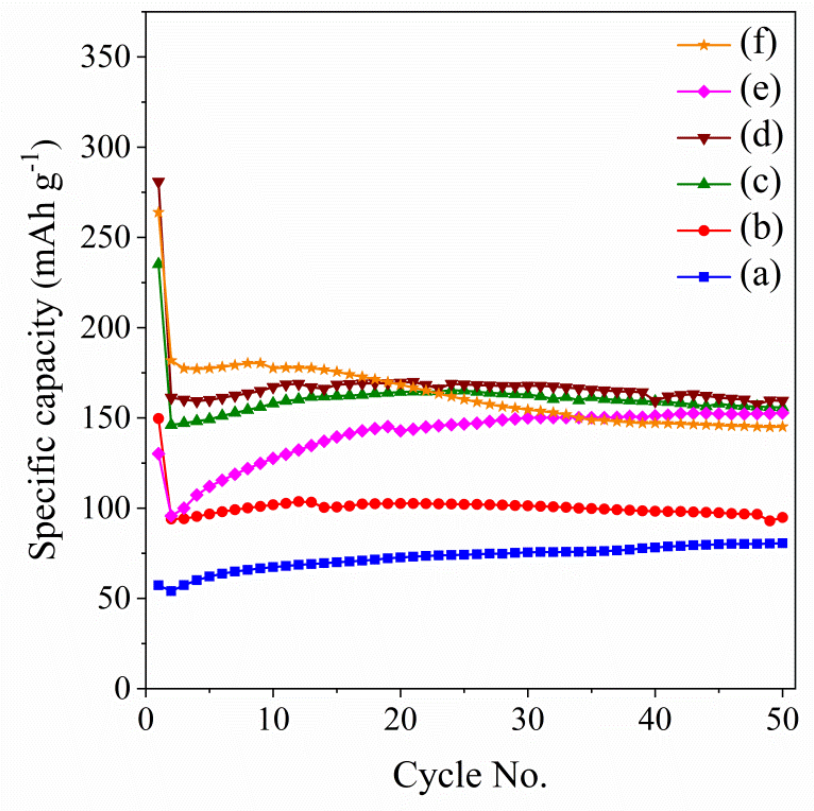

Figure 3.27 Long cycle performance of $LiFeBO_{3-x}F_{2x}$ for x = (a) 0, (b) 0.05, (c) 0.1, (d) 0.2, (e) 0.3, and (f) 0.5 at 1 C.

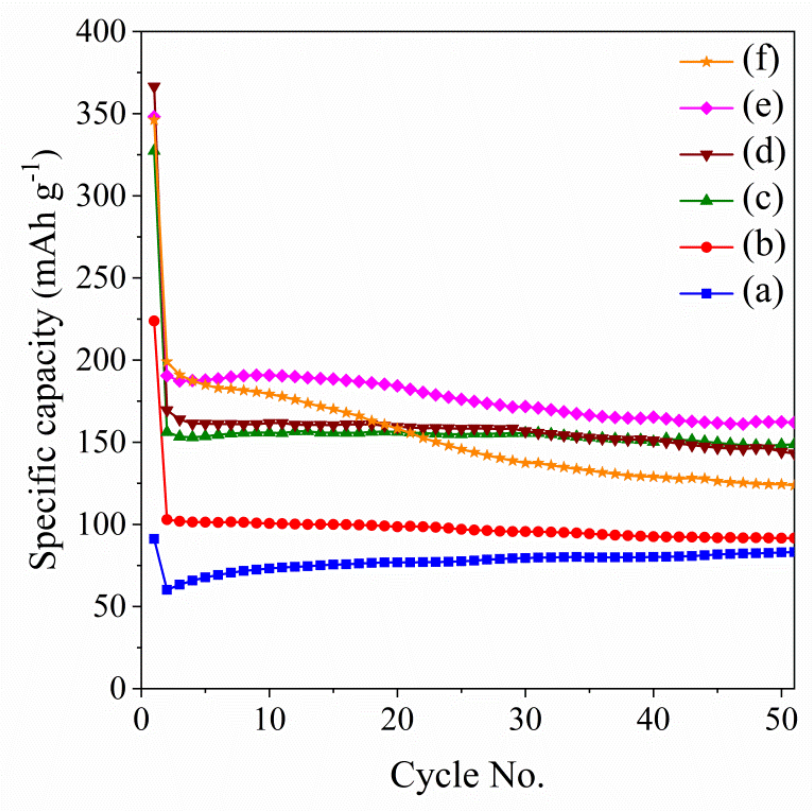

Figure 3.28 Long cycle performance of $LiFeBO_{3-x}F_{2x}$ for x = (a) 0, (b) 0.05, (c) 0.1, (d) 0.2, (e) 0.3, and (f) 0.5 at 0.05C as initial cycle and at 1 C as 2nd – 51st cycle.

3.6 *Ex-situ* x-ray diffraction of $LiFeBO_{3-x}F_{2x}$

Ex-situ XRD patterns of the LFeBF (x = 0.05, 0.1, 0.2, 0.3, and 0.5) after first cycle at 0.05C was observed to study about the high differences of capacity between first cycle with second cycle in electrochemical performance. *Ex-situ* XRD was showed the structure of LFeBF (x = 0.05, 0.1, 0.2, 0.3, and 0.5) after cycle. The differences XRD pattern before and after cycle was observed to solve the problem of electrochemical performance that decreased after first cycle.

Ex-situ XRD patterns of the LFeBF (x = 0.05, 0.1, 0.2, 0.3, and 0.5) after first cycle at 0.05C are showed in **Figure 3.29**. *Ex-situ* XRD pattern of LFeBF (x = 0.05) was showed match with peak of LFeB. For ex-situ XRD pattern of LFeBF (x = 0.1) was indicated match with LFeB and $LiBO_2$. For *ex-situ* XRD pattern of LFeBF (x = 0.2 and 0.3) showed match with peak of $LiBO_2$. *Ex-situ* XRD pattern of LFeBF (x = 0.5) indicated match with $Li_2B_4O_7$. There is also found an unknown impurities peak in the middle that indicated by asterisk mark. It is difficult to observed the LiF peak because the peak of LiF and Al foil that we used for current collector is overlaping.

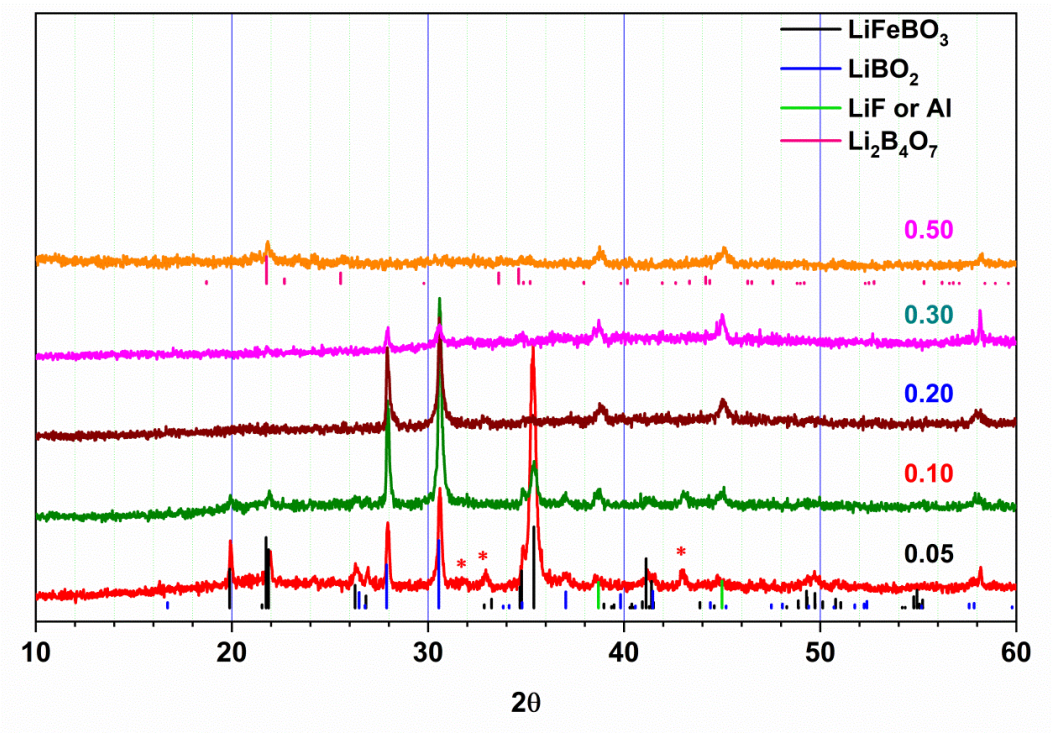

Figure 3.29 *Ex-situ* XRD patterns of $LiFeBO_{3-x}F_{2x}$ for 0, 0.05, 0.1, 0.2, 0.3, and 0.5 after first cycle at 0.05C.

4. Conclusions

Fluorine substituted $LiFeBO_{3-x}F_{2x}$ (x = 0, 0.05, 0.1, 0.2, 0.3, and 0.5) were successively synthesized using solid-state reaction method without any external carbon source. XRD patterns of LFeBF showed that increase in fluorine substitution ratio induced the structural changes of LFeBF from monoclinic to vonsenite . Moreover, in ^{7}Li MAS NMR spectra the isotropic peaks of LFeBF with high fluorine substitution ratio have shifted downfield that confirms the structural change from monoclinic, in which Li atoms are surrounded by trigonal bipyramidal $FeBO_3$, to vonsenite with Li atoms are surrounded by octahedral Fe_2BO_3. Both XRD and NMR studies are well agreed the structural change of LFeBF with high fluorine substitution ratio. The electrochemical property measured at 1.0 – 4.5 V for LFeBF (x = 0.3) shows the highest discharge capacity and stability in all C rates, which the initial discharge capacity is 363.98 mAh g^{-1} at 0.05 C rate with 165% of the theoretical capacity for LFeB with 220 mAh g^{-1}. This fluorine substituted LFeBF can be a new candidate of cathode material for LIBs due to higher discharge capacity compared to conventional carbon coated LFeB [19, 20, 22, 23, 35, 37, 38].

5. Reference

[1] H. Chen, T.N. Cong, W. Yang, C. Tan, Y. Li, Y. Ding, Progress in Natural Science, 19 (2009) 291-312.

[2] T. Kim, W. Song, D.-Y. Son, L.K. Ono, Y. Qi, Journal of Materials Chemistry A, 7 (2019) 2942-2964.

[3] J.M. Tarascon, M. Armand, Nature, 414 (2001) 359-367.

[4] Z. Gong, Y. Yang, Energy & Environmental Science, 4 (2011) 3223.

[5] M. Li, J. Lu, Z. Chen, K. Amine, Advanced Materials, 30 (2018) 1800561.

[6] B. Scrosati, Journal of Solid State Electrochemistry, 15 (2011) 1623-1630.

[7] J. Xu, S. Dou, H. Liu, L. Dai, Nano Energy, 2 (2013) 439-442.

[8] M.D. Bhatt, C. O'Dwyer, Physical Chemistry Chemical Physics, 17 (2015) 4799-4844.

[9] N. Nitta, F. Wu, J.T. Lee, G. Yushin, Materials Today, 18 (2015) 252-264.

[10] J.B. Goodenough, K.-S. Park, Journal of the American Chemical Society, 135 (2013) 1167-1176.

[11] E.K. Heidari, A. Kamyabi-Gol, M.H. Sohi, A. Ataie, Journal of Ultrafine Grained and Nanostructured Materials, 51 (2018) 1-12.

[12] M.S. Whitthingham, Chemical reviews, 104 (2004) 4271-4301.

[13] A.K. Padhi, K.S. Nanjundaswamy, J.B. Goodenough, Journal of the Electrochemical Society, 144 (1997) 1188-1194.

[14] Y. Janssen, D.S. Middlemiss, S.-H. Bo, C.P. Grey, P.G. Khalifah, Journal of the American Chemical Society, 134 (2012) 12516-12527.

[15] A. Yamada, N. Iwane, Y. Harada, S.-i. Nishimura, Y. Koyama, I. Tanaka, Advanced Materials, 22 (2010) 3583-3587.

[16] Y.Z. Dong, Y.M. Zhao, Z.D. Shi, X.N. An, P. Fu, L. Chen, Electrochimica Acta, 53 (2008) 2339-2345.

[17] V. Legagneur, Y. An, A. Mosbah, R. Portal, A.L.G.L. Salle, A. Verbaere, D. Guyomard, Y. Piffard, Solid State Ioics, 139 (2001) 37-46.

[18] M.A. Cambaz, M. Anji Reddy, B.P. Vinayan, R. Witte, A. Pohl, X. Mu, V.S.K. Chakravadhanula, C. Kübel, M. Fichtner, ACS Applied Materials & Interfaces, 8 (2016) 2166-2172.

[19] V.J. Gallegos-sanchez, L.C. Torres-Gonzalez, E.M. Sanchez, L.L. Garza-Tovar, Digest Journal of Nanomaterials and Biostructures, 11 (2016) 1063-1071.

[20] L. Tao, G. Rousse, J.N. Chotard, L. Dupont, S. Bruyère, D. Hanžel, G. Mali, R. Dominko, S. Levasseur, C. Masquelier, Journal of Materials Chemistry A, 2 (2014) 2060-2070.

[21] P. Barpanda, Y. Yamashita, Y. Yamada, A. Yamada, Journal of The Electrochemical Society, 160 (2013) A3095-A3099.

[22] X. Gu, M. Ting, S. Zhi, Journal of Sol-Gel Science and Technology, 81 (2016) 362-366.

[23] B. Zhang, L. Ming, J.-c. Zheng, J.-f. Zhang, C. Shen, Y.-d. Han, J.-l. Wang, S.-e. Qin, Journal of Power Sources, 261 (2014) 249-254.

[24] H.C. Shin, S.B. Park, H. Jang, K.Y. Chung, W.I. Cho, C.S. Kim, B.W. Cho, Electrochimica Acta, 53 (2008) 7946-7951.

[25] Y. Ge, X. Yan, J. Liu, X. Zhang, J. Wang, X. He, R. Wang, H. Xie, Electrochimica Acta, 55 (2010) 5886-5890.

[26] Y. Mi, C. Yang, Z. Zuo, L. Qi, C. Tang, W. Zhang, H. Zhou, Electrochimica Acta, 176 (2015) 642-648.

[27] X.-Z. Liao, Y.-S. He, Z.-F. Ma, X.-M. Zhang, L. Wang, Journal of Power Sources, 174 (2007) 720-725.

[28] B.C. Sin, L. Singh, J. An, H. Lee, H.-i. Lee, Y. Lee, Journal of Power Sources, 313 (2016) 112-119.

[29] B.C. Sin, L. Singh, J. Lee, Y. Lee, Journal of Electroanalytical Chemistry, 823 (2018) 155-160.

[30] Y. Deng, C. Yang, K. Zou, X. Qin, Z. Zhao, G. Chen, Advanced Energy Materials, 7 (2017) 1601958.

[31] Y.Z. Dong, Y.M. Zhao, P. Fu, H. Zhou, X.M. Hou, Journal of Alloys and Compounds, 461 (2008) 585-590.

[32] J.S. Swinnea, H. Steinfink, American Mineralogist, 68 (1983) 827-832.

[33] P. Barpanda, D. Dwibedi, S. Ghosh, Y. Kee, S. Okada, Ionics, 21 (2015) 1801-1812.

[34] S.-H. Bo, K.-W. Nam, O.J. Borkiewicz, Y.-Y. Hu, X.-Q. Yang, P.J. Chupas, K.W. Chapman, L. Wu, L. Zhang, F. Wang, C.P. Grey, P.G. Khalifah, Inorganic Chemistry, 53 (2014) 6585-6595.

[35] S.-H. Bo, F. Wang, Y. Janssen, D. Zeng, K.-W. Nam, W. Xu, L.-S. Du, J. Graetz, X.-Q. Yang, Y. Zhu, J.B. Parise, C.P. Grey, P.G. Khalifah, Journal of Materials Chemistry, 22 (2012) 8799.

[36] M.C. Tucker, M.M. Doeff, T.J. Richardson, R. Fiñones, J.A. Reimer, E.J. Cairns, Electrochemical and Solid-State Letters, 5 (2002) A95.

[37] D. Zhang, J. Qiao, X. Dong, B. Xu, R. Li, C. Chang, International Journal of Electrochemical Science, 13 (2018) 1744-1753.

[38] Z. Chen, L. Cao, L. Chen, H. Zhou, C. Zheng, K. Xie, Y. Kuang, Journal of Power Sources, 298 (2015) 355-362.